Chemical Ionization Mass Spectrometry Utilizing Ammonium Ions (NH_4^+ CIMS) for Measurements of Organic Compounds in the Atmosphere

Lu Xu[1,2], Matthew M. Coggon[2], Chelsea E. Stockwell[1,2], Jessica B. Gilman[2], Michael A. Robinson[1,2,3], Martin Breitenlechner[1,2], Aaron Lamplugh[1,2,*], John D. Crounse[4], Paul O. Wennberg[4,5], J. Andrew Neuman[1,2], Gordon A. Novak[1,2], Patrick R. Veres[2], Steven S. Brown[2,3], and Carsten Warneke[2]

[1]Cooperative Institute for Research in Environmental Sciences, University of Colorado Boulder, Boulder, Colorado, USA
[2]NOAA Chemical Sciences Laboratory, Boulder, Colorado, USA
[3]Department of Chemistry, University of Colorado Boulder, Boulder, Colorado, USA
[4]Division of Geological and Planetary Sciences, California Institute of Technology, Pasadena, CA, USA
[5]Division of Engineering and Applied Science, California Institute of Technology, Pasadena, CA, USA
[*]Now at Institute of Behavioral Science, University of Colorado Boulder, Boulder, Colorado, USA

Correspondence: Lu Xu (lu.xu@noaa.gov) and Carsten Warneke (carsten.warneke@noaa.gov)

Abstract. We describe the characterization and field deployment of a Chemical Ionization Mass Spectrometer (CIMS) using a recently developed focusing ion-molecule reactor (FIMR) and ammonium-water cluster ($NH_4^+ \cdot H_2O$) as the reagent ion (denoted as NH_4^+ CIMS). We show that $NH_4^+ \cdot H_2O$ is a highly versatile reagent ion for measurements of a wide range of oxygenated organic compounds. The major product ion is the cluster with NH_4^+ produced via ligand-switching reactions. Other product ions (e.g., protonated ion, cluster ion with $NH_4^+ \cdot H_2O$, with H_3O^+, and with $H_3O^+ \cdot H_2O$) are also produced, but with minor fractions for most of the oxygenated compounds studied here. The instrument sensitivities (ion counts per second per part per billion by volume, cps $ppbv^{-1}$) and product distributions are strongly dependent on the instrument operating conditions, including the ratio of ammonia (NH_3) and H_2O flows and the drift voltages, which should be carefully selected to ensure $NH_4^+ \cdot H_2O$ as the predominant reagent ion and to optimize sensitivities. For monofunctional analytes, the $NH_4^+ \cdot H_2O$ chemistry exhibits high sensitivity (i.e., > 1000 cps $ppbv^{-1}$) towards ketones, moderate sensitivity (i.e., between 100 and 1000 cps $ppbv^{-1}$) towards aldehdyes, alcohols, organic acids, and monoterpenes, low sensitivity (i.e., between 10 and 100 cps $ppbv^{-1}$) towards isoprene and C1 and C2 organics, and negligible sensitivity (i.e., < 10 cps $ppbv^{-1}$) towards reduced aromatics. The instrumental sensitivities of analytes depend on the binding energy of the analyte-NH_4^+ cluster, which can be estimated using voltage scanning. This offers the possibility to constrain the sensitivity of analytes for which no calibration standards exist. This instrument was deployed in the RECAP campaign (Re-Evaluating the Chemistry of Air Pollutants in California) in Pasadena, California during summer 2021. Measurement comparisons against co-located mass spectrometers show that the NH_4^+ CIMS is capable of detecting compounds from a wide range of chemical classes. The NH_4^+ CIMS is valuable for quantification of oxygenated VOCs and is complementary to existing chemical ionization schemes.

1 Introduction

Quantifying atmospheric volatile organic compounds (VOCs) and their oxidation products is critical for understanding the formation of ozone (O_3) and organic aerosol (OA). However, this objective has been a longstanding challenge because of the sheer number and significant chemical complexity of organic compounds in the atmosphere (Goldstein and Galbally, 2007). Chemical ionization mass spectrometry (CIMS) is a widely used and rapidly developing technique to characterize atmospheric trace gases. The advantages of CIMS include fast time response, high selectivity and sensitivity, and detection linearity over a wide range of analyate mixing ratios. In CIMS, the analytes are ionized via ion-molecule reactions with a reagent ion, which is soft and largely preserves the identity of the analytes. The detection capability of CIMS depends on the selection of reagent ions, which are sensitive towards different classes of organics. The commonly employed reagent ions include H_3O^+ to detect reduced and small functionalized VOCs (de Gouw and Warneke, 2007), I^- to detect inorganics and polar and acidic organics (Lee et al., 2014a; Robinson et al., 2022), CF_3O^- to detect organic peroxides and other multifunctional organics (Crounse et al., 2006; Xu et al., 2020), SF_6^- to detect organic acids (Nah et al., 2018), NO_3^- to detect highly oxygenated molecules (Ehn et al., 2014), and protonated amines to detect reactive radicals (Berndt et al., 2018). Exploring novel reagent ions is an active research area to expand the detection capability of CIMS and to provide precise measurements of atmospheric species with high sensitivity. These efforts enable a comprehensive description of the complex mixture of atmospheric organic compounds.

One ionization scheme under active development utilizes the ammonium ion (NH_4^+) chemistry. Several recent studies have demonstrated its capability to detect a range of oxygenated organic compounds, including alcohols, aldehydes, ketones, and even the short-lived peroxy radicals (RO_2) (Blake et al., 2006; Lindinger et al., 1998; Canaval et al., 2019; Hansel et al., 2018; Müller et al., 2020; Zaytsev et al., 2019; Berndt et al., 2018; Khare et al., 2022). One reason NH_4^+ chemistry is attractive is that it detects oxygenated organic compounds in the positive mass spectrometer mode, in contrast to existing reagent ions (i.e., I^-, CF_3O^-, and NO_3^-) which are operated in negative mode. This offers the potential to rapidly switch between NH_4^+ and H_3O^+ within the same instrument to detect both oxygenated and reduced organic compounds, respectively, without substantial alteration of the electric fields in the mass spectrometer. Zaytsev et al. (2019) and Müller et al. (2020) demonstrated the feasibility of such rapid switching in laboratory conditions. The application of NH_4^+ CIMS in recent studies has largely focused on laboratory studies (Berndt et al., 2018; Zaytsev et al., 2019), but its deployment in field measurements and inter-comparison with other analytical instruments are scarce (Khare et al., 2022).

The instrument design, including the ion source and the ion-molecule reactor (IMR), differs between studies. Hansel et al. (2018) applied NH_4^+ ion chemistry in a PTR3 instrument (Breitenlechner et al., 2017) (i.e., NH_4^+ – PTR3) and detected peroxy radicals and other products from cyclohexene ozonolysis with sensitivities up to 2.8×10^4 cps ppbv^{-1} in a free-jet flow system. Using a similar instrument, Zaytsev et al. (2019) calibrated 16 compounds, with a maximum sensitivity of 8.9×10^4 cps ppbv^{-1} for decanone. In both studies, the major reagent ion is $NH_4^+ \cdot H_2O$, generated in a corona discharge ion source from a mixture of NH_3 and H_2O gas. Later, Müller et al. (2020) developed a method to produce NH_4^+ using a mixture of water vapor and nitrogen in a hollow cathode glow discharge ion source, which is used in PTR-MS instruments with a traditional drift tube design that includes extraction plates between the hollow cathode ion source and drift tube. Canaval et al. (2019) used a Selective Reagent

Ionization Time-of-Flight Mass Spectrometer (SRI-ToF-MS) to produce NH_4^+ via reaction of He^+ and gas NH_3. Different instrument designs affect the distribution of reagent ions (i.e., NH_4^+ vs $NH_4^+ \cdot H_2O$ vs $NH_4^+ \cdot NH_3$), detection efficiency, and sensitivity.

In this study, we describe the performance of a NH_4^+ CIMS using a Tofwerk Vocus long Time-of-Flight Mass Spectrometer (Krechmer et al., 2018). We investigate the impacts of instrument conditions on the distribution of reagent ions and the instrumental sensitivities of 60 analytes from several chemical functional classes. Building upon extensive calibrations, we explore the dependence of sensitivity on the ion-molecule reaction rate constant and the binding energy of analyte-NH_4^+ cluster, aiming to derive a relationship to approximate the sensitivity of analytes for which no calibration standards exist. Further, this instrument was deployed during the RECAP campaign (Re-Evaluating the Chemistry of Air Pollutants in California) in Pasadena, California during the summer of 2021. The instrument performance is further evaluated by comparison to several co-located mass spectrometers.

2 Experimental Methods

2.1 Instrument Description

The instrument in this work is based on the Tofwerk Vocus, which utilizes a new ion source, a focusing ion-molecule reactor (FIMR), and a long Time-of-Flight Mass Spectrometer (LToF). A detailed description of the Vocus can be found in Krechmer et al. (2018). Here we briefly summarize the generation of reagent ions and instrument operation conditions.

The chemical ionization gas entering the ion source is produced by mixing NH_3 and H_2O from two streams: a 20 sccm flow of water vapor from the headspace of a liquid water reservoir (denoted as H_2O flow) and an additional 1 sccm from the headspace of a reservoir containing 0.5% (vol %) ammonium hydroxide water solution (denoted as NH_3 flow, which contains both NH_3 and H_2O). The ion source consists of two conical surfaces with a voltage gradient. A plasma is produced between the conical surfaces, which primarily ionizes water molecules producing H_3O^+. The discharge current is regulated at 2.0 mA. Because NH_3 has a larger proton affinity than H_2O, the proton transfer reaction (Eqn. 1) produces NH_4^+, which then readily clusters with abundant H_2O to produce the targeted reagent ion $NH_4^+ \cdot H_2O$ (Eqn. 2). Besides H_2O, NH_4^+ can also cluster with NH_3 to produce $NH_4^+ \cdot NH_3$ (Eqn. 3). The abundance of H_2O in the ion source also leads to formation of $H_3O^+ \cdot (H_2O)_n$ cluster ions (Eqn. 4). Overall, several ions, $NH_4^+ \cdot X_n$ (ligand X = NH_3 and H_2O, n = 0,1,2) and $H_3O^+ \cdot (H_2O)_n$, are generated from the ion source and can potentially serve as reagent ions.

$$H_3O^+ + NH_3 \rightarrow NH_4^+ + H_2O \tag{1}$$

$$NH_4^+ + nH_2O \rightarrow NH_4^+ \cdot (H_2O)_n \tag{2}$$

$$NH_4^+ + nNH_3 \rightarrow NH_4^+ \cdot (NH_3)_n \quad (3)$$

$$H_3O^+ + nH_2O \rightarrow H_3O^+ \cdot (H_2O)_n \quad (4)$$

The reagent gas flow pushes the ions into the FIMR where they subsequently react with analytes. Sample air enters the FIMR through a 25 mm long PEEK capillary (ID 0.18 mm). The sample flow rate is ∼100 sccm, at a FIMR pressure of 3 mbar in this study. The FIMR is a 100 mm long glass tube with an inner diameter of 10 mm. A quadrupole radio frequency (RF) field is applied to the FIMR to collimate ions into a narrow beam significantly enhancing the sensitivity (Krechmer et al., 2018). The FIMR conditions, including temperature, pressure, drift voltage, and the ratio of NH_3 to H_2O into the ion source, all control the degree of cluster-ion formation, the distribution of reagent ions, and ultimately the sensitivity, as will be discussed in section 3.2 and 3.3. Ions from the FIMR travel through a big segmented quadrupole (BSQ). The BSQ serves as a high-pass band filter to reduce the signal intensity of reagent ions while simultaneously guiding ions into the time-of-flight mass spectrometer. As a result of this filtering, the observed distribution of reagent ions is not the same as the actual distribution in the FIMR (Krechmer et al., 2018). After the BSQ, the ions travel through the primary beam region and eventually are detected by the long time-of-flight mass spectrometer with a mass resolution (full width at half maximum, FWHM) up to 8000 at m/Q 100. The extraction frequency of the ToF is set at 17.5 kHz.

2.2 Laboratory Characterization

We calibrate the instrumental sensitivities (cps $ppbv^{-1}$) of 60 organic compounds (Table 1) using two methods, standard gas cylinders (SGC) and a home-built liquid calibration unit using either water or hexane as solvent (LCU-W and LCU-H), as described in Supplement S1. We find minimal dependence of sensitivity on sample relative humidity (RH) as shown in Figure S1, consistent with Khare et al. (2022) and observations made when running the Vocus in H_3O^+ mode (Krechmer et al., 2018). This is mainly because a large amount of water vapor (20 sccm) is deliberately added to the FIMR. As an example, the water amount in 100 sccm ambient sample under 25°C and 100% RH is only 15% of the added 20 sccm water vapor to the FIMR, assuming no water vapor loss in both processes. The instrument background is determined by passing ambient air through a platinum catalytic converter heated to 400 °C. The detection limit is defined as three standard deviations of measurement background for 1 s integration time.

During transport, ions get lost in the BSQ, in the ion guides, and in the extraction region of the ToF. We quantify the mass-dependent transmission efficiency relative to the reagent ion $NH_4^+ \cdot H_2O$ by introducing a series of compounds spanning a range of molecular weight (32 - 370 m/Q) in a large enough quantity to deplete the fraction of reagent ions by ∼20-30% (Huey et al., 1995; Heinritzi et al., 2016). The ratio of the increase of the product ions to the decrease of the reagent ion indicates the relative transmission efficiency between these two masses. A detailed derivation can be found in the Supplement S1.

We have performed laboratory tests and measured the product distribution of 60 organic compounds. The product ions are identified by sampling the headspace of a small vial containing pure analyte. A distance is kept between the instrument inlet

and the vial to keep analyte concentration low. Ions correlating with the parent ion ($NH_4^+ \cdot A$) with r^2 larger than 0.95 and accounting for larger than 1% of the parent ion signal are considered as product ions from the analyte. The distribution of product ions depends on the distribution of reagent ions. In this test, we maintain the $NH_4^+ \cdot H_2O/H_3O^+ \cdot H_2O$ ratio between 5 and 20. Under this condition, the ion chemistry of $H_3O^+ \cdot (H_2O)_n$ is negligible.

To probe the stability of product ions, we performed voltage scanning tests following the procedure outlined in Lopez-Hilfiker et al. (2016) and Zaytsev et al. (2019). In brief, we vary the voltage gradient (ΔV) between FIMR back and skimmer while keeping the voltage gradient between FIMR front and back constant. A larger ΔV increases the collisional energy, causes stronger collision-induced dissociation of product ions, and tends to decrease the signal of product ions. We define ΔV_{50} as the voltage gradient at which the parent ion $NH_4^+ \cdot A$ signal drops to half of the maximum signal. This ΔV_{50} represents the electric field required to break each $NH_4^+ \cdot A$ and therefore is related to the binding energy of $NH_4^+ \cdot A$. Further, ΔV_{50} is converted to the kinetic energy of $NH_4^+ \cdot A$ in the center of mass (i.e., $KE_{cm,50}$) using a parameterization of mass-dependent ion-mobility (Zaytsev et al. (2019) and details in the Supplement S1). $KE_{cm,50}$ is a measure of the $NH_4^+ \cdot A$ stability.

Table 1: Sensitivities (cps $ppbv^{-1}$), background (cps), and detection limits (pptv for a 1 s integration time) of NH_4^+ CIMS

Species	Ion Formula	Ion m/Q	Sensitivity	Background	LOD	Methods
Methanol	$NH_4^+ \cdot CH_4O$	50.06	<1	5	2.5e4	SGC, LCU-W
Acetonitrile	$NH_4^+ \cdot C_2H_3N$	59.06	5.5e2	1.3e2	85	SGC, LCU-W
Acetaldehyde	$NH_4^+ \cdot C_2H_4O$	62.06	21	2.5e2	3.2e3	SGC, LCU-H
Ethylene oxide	$NH_4^+ \cdot C_2H_4O$	62.06	<1	2.5e2	2.0e5	SGC
Ethanol	$NH_4^+ \cdot C_2H_6O$	64.08	7	1.5e2	6.9e3	SGC, LCU-W
Propionitrile	$NH_4^+ \cdot C_3H_5N$	73.11	1.8e3	N/A	N/A	SGC
Acrolein	$NH_4^+ \cdot C_3H_4O$	74.06	2.1e2	31	1.7e2	SGC
Acetone	$NH_4^+ \cdot C_3H_6O$	76.08	1.2e3	4.7e3	2.3e2	SGC, LCU-W
Propanal	$NH_4^+ \cdot C_3H_6O$	76.08	1.0e2	4.7e3	2.8e3	SGC
Acetic Acid	$NH_4^+ \cdot C_2H_4O_2$	78.05	25	3.6e2	3.9e3	LCU-W
2-propanol	$NH_4^+ \cdot C_3H_8O$	78.09	90	23	2.9e2	LCU-W
Ethylene Glycol	$NH_4^+ \cdot C_2H_6O_2$	80.07	1.0e3	95	38	LCU-W
Furan	$NH_4^+ \cdot C_4H_4O$	86.06	<1	13	4.4e4	SGC, LCU-H
Isoprene	$NH_4^+ \cdot C_5H_8$	86.10	28	2	1.7e2	SGC
MVK	$NH_4^+ \cdot C_4H_6O$	88.08	1.5e3	40	18	SGC, LCU-W
MACR	$NH_4^+ \cdot C_4H_6O$	88.08	3.3e2	40	84	SGC, LCU-H
MEK	$NH_4^+ \cdot C_4H_8O$	90.14	1.6e3	92	22	SGC
Tetrahydrofuran	$NH_4^+ \cdot C_4H_8O$	90.14	8.2e2	92	44	SGC
Propanoic Acid	$NH_4^+ \cdot C_3H_6O_2$	92.07	3.1e2	2.9e2	2.3e2	LCU-W

Continued on next page

Table 1 – continued from previous page

Species	Ion Formula	Ion m/Q	Sensitivity	Background	LOD	Methods
Hydroxyacetone	$NH_4^+ \cdot C_3H_6O_2$	92.07	2.1e3	2.9e2	35	SGC, LCU-W
2-butanol	$NH_4^+ \cdot C_4H_{10}O$	92.11	1.9e2	4	47	LCU-W
1,3-propanediol	$NH_4^+ \cdot C_3H_8O_2$	94.09	1.0e3	3.6e2	68	LCU-W
Benzene	$NH_4^+ \cdot C_6H_6$	96.08	<1	3	9.3e3	SGC, LCU-H
2-methylfuran	$NH_4^+ \cdot C_5H_6O$	100.08	37	18	4.8e2	SGC, LCU-H
Methacrylic Acid	$NH_4^+ \cdot C_4H_6O_2$	104.07	97	1.6e2	5.0e2	LCU-W
Pentanal	$NH_4^+ \cdot C_5H_{10}O$	104.11	2.2e2	22	90	LCU-H
3-Pentanone	$NH_4^+ \cdot C_5H_{10}O$	104.11	2.9e3	22	7	LCU-H
2-Pentanone	$NH_4^+ \cdot C_5H_{10}O$	104.11	2.8e3	22	7	SGC
2,3-butanedione	$NH_4^+ \cdot C_4H_6O_2$	104.12	2.6e2	1.6e2	1.8e2	LCU-W
Butyric Acid	$NH_4^+ \cdot C_4H_8O_2$	106.09	1.8e2	74	2.0e2	LCU-W
2-pentanol	$NH_4^+ \cdot C_5H_{12}O$	106.12	3.0e2	2	19	LCU-W
Toluene	$NH_4^+ \cdot C_7H_8$	110.10	<1	2	1.3e4	SGC, LCU-H
Phenol	$NH_4^+ \cdot C_6H_6O$	112.08	1.9e2	19	1.2e2	SGC, LCU-H
Furfural	$NH_4^+ \cdot C_5H_4O_2$	114.06	3.3e3	15	5	SGC
2-hexanone	$NH_4^+ \cdot C_6H_{12}O$	118.12	3.8e3	10	4	SGC, LCU-H
2,3-Pentanedione	$NH_4^+ \cdot C_5H_8O_2$	118.15	4.9e2	80	76	SGC, LCU-W
Hexanal	$NH_4^+ \cdot C_6H_{12}O$	118.19	7.5e2	10	18	LCU-H
1-hexanol	$NH_4^+ \cdot C_6H_{14}O$	120.14	1.4e2	1	36	LCU-W
Benzonitrile	$NH_4^+ \cdot C_7H_5N$	121.08	3.7e3	2	3	SGC, LCU-H
Styrene	$NH_4^+ \cdot C_8H_8$	122.10	4.2e2	4	29	SGC
Benzaldehyde	$NH_4^+ \cdot C_7H_6O$	124.08	1.9e3	6	30	SGC, LCU-H
o-xylene	$NH_4^+ \cdot C_8H_{10}$	124.11	<1	2	4.5e4	SGC
m-xylene	$NH_4^+ \cdot C_8H_{10}$	124.11	<1	2	2.1e4	SGC
2-methylphenol	$NH_4^+ \cdot C_7H_8O$	126.09	2.5e2	5	48	SGC
heptanal	$NH_4^+ \cdot C_7H_{14}O$	132.22	6.5e2	6	15	LCU-H
2-heptanone	$NH_4^+ \cdot C_7H_{14}O$	132.22	3.5e3	6	3	LCU-H
1,2,4-TMB	$NH_4^+ \cdot C_9H_{12}$	138.13	<1	0.6	2.2e3	SGC
Naphthalene	$NH_4^+ \cdot C_{10}H_8$	146.20	6	1.5	1.9e3	SGC
Octanal	$NH_4^+ \cdot C_8H_{16}O$	146.24	8.0e2	5	11	LCU-H
2-octanone	$NH_4^+ \cdot C_8H_{16}O$	146.24	2.9e3	5	3	LCU-H
p-cymeme	$NH_4^+ \cdot C_{10}H_{14}$	152.25	9	0.8	4.0e2	SGC

Continued on next page

Table 1 – continued from previous page

Species	Ion Formula	Ion m/Q	Sensitivity	Background	LOD	Methods
Limonene	$NH_4^+ \cdot C_{10}H_{16}$	154.16	3.9e2	2	11	SGC, LCU-H
α-pinene	$NH_4^+ \cdot C_{10}H_{16}$	154.16	3.6e2	2	12	LCU-H
β-pinene	$NH_4^+ \cdot C_{10}H_{16}$	154.16	4.6e2	2	9	SGC
Camphene	$NH_4^+ \cdot C_{10}H_{16}$	154.16	3.4e2	2	13	SGC
Nonanal	$NH_4^+ \cdot C_9H_{18}O$	160.27	6.5e2	7	18	LCU-H
2-nonanone	$NH_4^+ \cdot C_9H_{18}O$	160.27	2.6e3	7	4	LCU-H
α-pinene oxide	$NH_4^+ \cdot C_{10}H_{16}O$	170.27	1.1e3	2	4	LCU-H
Texanol	$NH_4^+ \cdot C_{12}H_{24}O_3$	234.21	9.0e2	2	6	LCU-W
D5-siloxane	$NH_4^+ \cdot C_{10}H_{30}O_5Si_5$	388.81	6.2e3	5	1	SGC, LCU-H

2.3 Field Deployment

The NH_4^+ CIMS was deployed during the RECAP campaign (Re-Evaluating the Chemistry of Air Pollutants in California) in Pasadena, California from August-September, 2021. The ground sampling site is located on the campus of the California Institute of Technology, which is only one block away from the original sampling site during the 2010 CalNex study (Ryerson et al., 2013). The instrument inlet was set up on a tower 10 m above the ground. The instrument was operated to sample gas phase from August 10th to 19th. Later, the instrument was coupled to a Vocus Inlet for Aerosol (VIA) to automatically switch sampling between gas and particle phases. This study will focus on the gas phase sampling period. Co-located instruments of relevance to this study include a Proton-Transfer-Reaction Mass Spectrometer (PTR-MS) (Yuan et al., 2016; de Gouw and Warneke, 2007) and a Gas-Chromatography Mass Spectrometer (GC-MS) (Lerner et al., 2017). A CF_3O^- Chemical Ionization Mass Spectrometer (CF_3O^- CIMS) (Crounse et al., 2006; Allen et al., 2022) was deployed at a different site on campus which is ∼800 m away from the NH_4^+ CIMS.

3 Instrument Performance

3.1 Overview of Ion Chemistry

The target primary reagent ion is $NH_4^+ \cdot H_2O$, which ionizes analyes (A) primarily via ligand-switching reactions (Eqn. 5) to form product ion $NH_4^+ \cdot A$. As analogous to proton affinity, we define NH_4^+ affinity as the negative of the enthalpy change in the reaction between NH_4^+ and an analyte. If an analyte has a larger NH_4^+ affinity than H_2O, reaction 5 is exothermic and will occur at a rate close to the collision limit when the difference in NH_4^+ affinity is sufficiently large (Adams et al., 2003). Otherwise, the ligand-switching reaction is endothermic. The energy imparted via the drift voltage could aid the endothermic reaction to overcome the energy barrier, but the instrument sensitivity in these instances is expected to be low. Besides the

target primary ion $NH_4^+ \cdot H_2O$, ions $NH_4^+ \cdot X_n$ (X = NH_3 and H_2O) and $H_3O^+ \cdot (H_2O)_n$ (n = 0,1,2) are observed, because the chemical ionization gas supply is a mixture of NH_3 and H_2O. These ions can also serve as reagent ions. Compared to NH_4^+, $NH_4^+ \cdot H_2O$ ionization is softer, because the H_2O acts as a third-body which dissipates some reaction energy. The reactivities of $NH_4^+ \cdot H_2O$ and $NH_4^+ \cdot NH_3$ are also expected to be different, as the NH_3 has a larger NH_4^+ affinity than H_2O (i.e., 108 vs 86 kJ mol^{-1}, NIST Chemistry WebBook). Therefore, the presence of multiple reagent ions will complicate the ionization chemistry and the interpretation of the mass spectra. To avoid such complication, the instrument conditions need to be carefully optimized to ensure $NH_4^+ \cdot H_2O$ exists as the dominant ion reacting with analytes.

$$NH_4^+ \cdot H_2O + A \rightarrow NH_4^+ \cdot A + H_2O \quad (5)$$

3.2 Modeling the Distribution of Reagent Ions

The distribution of the reagent ions is controlled by several factors, including the FIMR reduced electric field (E/N), temperature (T), pressure (P), the H_2O mixing ratio (χ_{H_2O}), and the ratio of NH_3 to H_2O (NH_3/H_2O). Many of these factors are interdependent - e.g., the E/N depends on pressure and temperature. To unravel the influences of these factors on the distribution of reagent ions, we develop a kinetic model. The model includes a series of reactions between two ions (NH_4^+ and H_3O^+) and two neutral molecules (NH_3 and H_2O). Clusters containing up to three molecules are considered, which leads to a total of 14 different ion clusters (Figure S4). The ion-molecule cluster reaction rate constant (i.e., forward reaction with $k_{forward}$) is calculated using the parameterization in Su (1994), assuming the reaction proceeds at the collision limit. The reaction rate constant of the declustering reaction (i.e., reverse reaction with $k_{reverse}$) is calculated using $k_{forward}$ and the equilibrium constant K_{eq}. $k_{reverse}$ for reaction 6, for example, is expressed by Eqn. 7, where M_0 represents the number density (cm^{-3}) under standard condition and K_{eq} represents the reaction equilibrium constant. K_{eq} is calculated using Eqn. 8, where ΔH^0 and ΔS^0 represent the enthalpy and entropy changes of the reaction at standard condition, respectively (Table S1), and T_{eff} represents the effective temperature of the ions in the FIMR. T_{eff} is calculated using Eqn. 9 (de Gouw et al., 2003), where k_B is the Boltzmann constant, m_{I^+}, m_A, and m_{buffer} are the masses of the ion I^+, the neutral analyte A, and the buffer gas, respectively, and the ν_d is the drift velocity of ion IA^+. ν_d is calculated using Eqn. 10, where μ_0 is the reduced mobility of IA^+ and calculated based on the parameterization in Steiner et al. (2014), P and T are the FIMR pressure and temperature, respectively, and E is the electric field strength across the FIMR.

$$I^+ + A \underset{k_{reverse}}{\overset{k_{forward}}{\rightleftharpoons}} IA^+ \quad (6)$$

$$k_{reverse} = \frac{k_{forward} \times M_0}{K_{eq}} \quad (7)$$

$$K_{eq} = \exp\left(-\frac{\Delta H^0}{RT_{eff}} + \frac{\Delta S^0}{R}\right) \quad (8)$$

$$\frac{3}{2}k_B T_{eff} = \frac{3}{2}k_B T_{FIMR} + \frac{(m_{I^+} + m_{buffer})m_A}{(m_{I^+} + m_A)}\frac{v_d^2}{2} \quad (9)$$

$$v_d = \mu_0 \frac{P_0}{P}\frac{T}{T_0}E \quad (10)$$

The influences of different FIMR conditions (i.e., E/N, T, P, χ_{H_2O}, and NH_3/H_2O) on the distribution of reagent ions are intertwined. To visualize their impacts, we first conduct simulations covering wide ranges of all five factors to locate the condition yielding the largest fraction of $NH_4^+ \cdot H_2O$ in total ions (denoted as $f_{NH_4^+ \cdot H_2O}$). The optimized condition is E/N = 60 Td (Townsend), T = 330 K, P = 5 mbar, χ_{H_2O} = 0.25, and NH_3/H_2O = 0.1%. Then, we conduct simulations using the optimal condition as a start point and vary one factor at a time while holding the other four constant, to investigate the impact of each factor on the distribution.

The simulation results are shown in Figure 1. Figure 1a shows that the reduced electric field (E/N) strongly impacts the distribution of reagent ions. When the E/N is below 40 Td, $H_3O^+ \cdot (H_2O)_3$ is the dominant ion, because the electric field is too weak to decluster. When the E/N is above 80 Td, NH_4^+ is dominant, because the electric field results in strong declustering and because NH_3 has higher proton affinity than H_2O. Only within a narrow E/N window (50 - 65 Td) is the target reagent ion $NH_4^+ \cdot H_2O$ the most abundant ion. Within this window, several other ions also exist, including NH_4^+, $NH_4^+ \cdot NH_3$, and $NH_4^+ \cdot (H_2O)_2$. The FIMR P and T impact the distribution (Figure 1b and c) through a similar mechanism as E/N, as smaller P and larger T results in larger E/N. As a result, $f_{NH_4^+ \cdot H_2O}$ also exhibits a non-monotonic dependence on the FIMR P and T. The impact of H_2O mixing ratio in the FIMR (χ_{H_2O}) on the distribution is shown in Figure 1d. The $f_{NH_4^+ \cdot H_2O}$ initially increases with the χ_{H_2O}, reaches a maximum when χ_{H_2O} is roughly 0.16-0.18, and then decreases with increasing χ_{H_2O}. This trend is because low χ_{H_2O} limits the supply of H_2O to cluster with NH_4^+ and high χ_{H_2O} favors the formation of larger clusters. To illustrate, Figure 1d shows that as χ_{H_2O} increases, the fraction of smaller clusters (i.e., $NH_4^+ \cdot H_2O$) decreases, but the fraction of larger clusters (i.e., $NH_4^+ \cdot (H_2O)_2$ and $NH_4^+ \cdot (H_2O)_3$) increases. Lastly, the NH_3/H_2O ratio has a strong impact on the cluster ion distribution (Figure 1e). Low NH_3/H_2O ratio (< 0.2%) results in insufficient supply of NH_4^+ and therefore $H_3O^+ \cdot (H_2O)_n$ ions dominate. High NH_3/H_2O ratio (> 0.55%) causes NH_4^+ to mainly cluster with NH_3, producing large amounts of $NH_4^+ \cdot NH_3$.

Evaluation of the kinetic simulation results by experimental observations is desirable, but challenging. One challenge is that the distribution of reagent ions can not be measured, because the BSQ serves as a high-pass band filter which reduces the signal intensity of reagent ions. Another challenge is that voltages in the ion transfer region between the drift tube and the mass analyzer can change the distribution of reagent ions, which causes the measured distribution different from that in the FIMR (Krechmer et al., 2018; Breitenlechner et al., 2022; Yuan et al., 2016). Overall, the simulation results illustrate the controlling effects of FIMR conditions on the distribution of reagent ions. The determination of FIMR conditions is eventually based on experimental calibration of instrumental sensitivity, which can be guided by the modeled distribution of reagent ions, as discussed in next section.

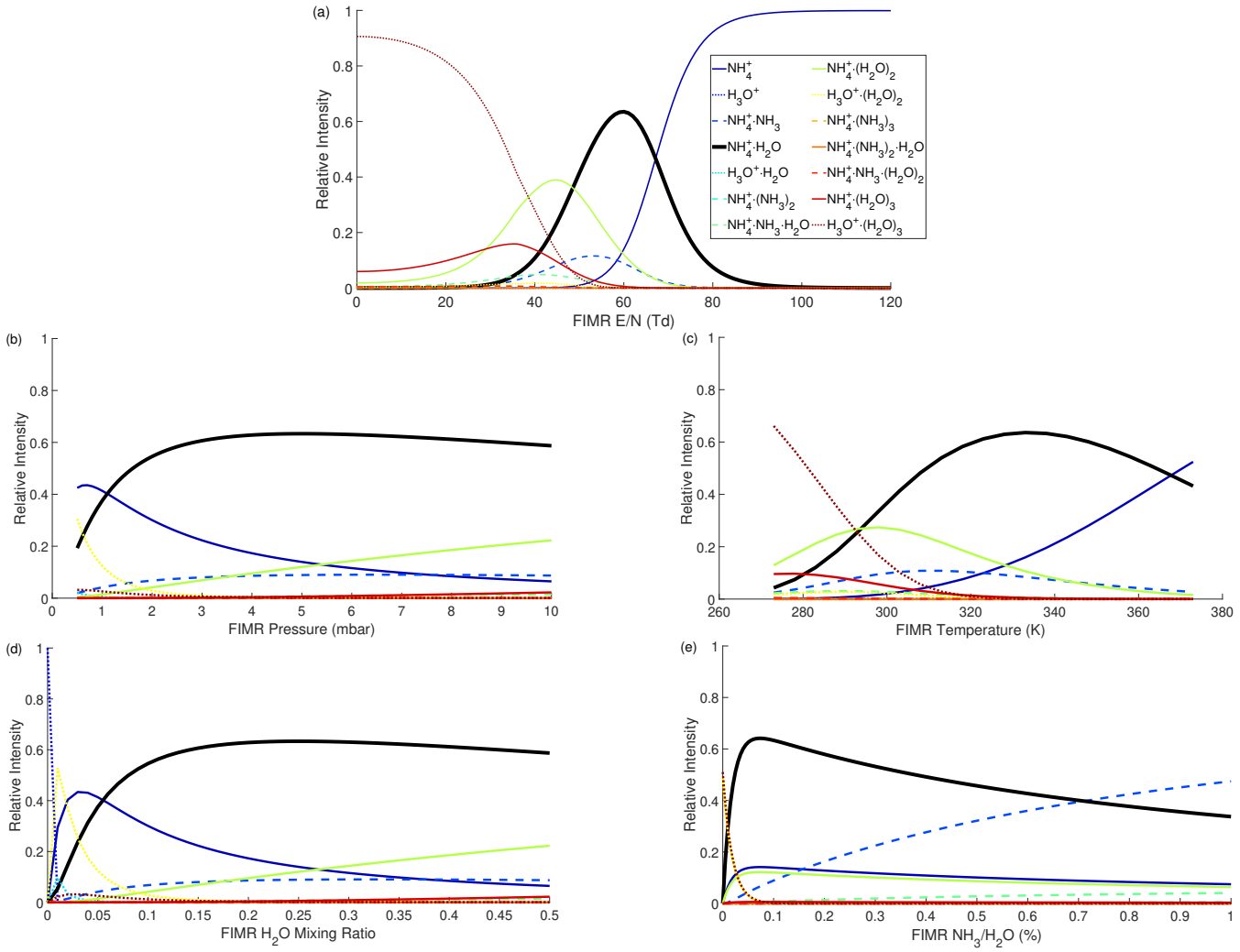

Figure 1. The dependence of modeled distribution of reagent ions on FIMR conditions. (a) E/N; (b) P; (c) T; (d) H_2O mixing ratio; (e) NH_3/H_2O. In each panel, the other four factors are held constant at the following conditions: E/N = 60 Td, P = 5 mbar, T = 330 K, H_2O mixing ratio = 0.25, NH_3/H_2O = 0.1%. Because the impacts of these factors are intertwined, each panel will change if the other four factors are at different values, as an example shown in Figure S5.

3.3 Dependence of sensitivities on FIMR conditions

While the above section modeled the dependence of the distribution of reagent ions on FIMR conditions, in this section we experimentally evaluate the dependence of analyte sensitivities on FIMR conditions. The analyte sensitivity depends not only on the distribution of reagent ions, but also other factors, including the number density of analytes in the FIMR, ion-molecular reaction time, stability of the product ion, and the transmission efficiency of product ions, as discussed below. Similar to the analysis in kinetic modeling, we experimentally vary one factor while holding the others constant.

Figure 2a shows the impacts of E/N on sensitivities of representative analytes. The E/N is varied by ramping the FIMR front voltage from 100 to 600 V, while holding the FIMR back voltage at 5 V. Under a FIMR pressure and temperature of 3 mbar and 313 K, respectively, the E/N ranges from 13 to 83 Td. The dependence of sensitivities on E/N follows a similar trend of the modeled distribution of $NH_4^+ \cdot H_2O$ (Figure 1a). The sensitivities initially increase with increasing E/N, partly because of more reagent ion $NH_4^+ \cdot H_2O$. As E/N keeps increasing, $NH_4^+ \cdot H_2O$ declusters into NH_4^+, so less $NH_4^+ \cdot H_2O$ causes a decrease in sensitivities. Besides changing the distribution of the reagent ions, changing E/N influences the sensitivity via other mechanisms, including the extent of declustering of $NH_4^+ \cdot A$ and the focusing effect of ions in the FIMR. Krechmer et al. (2018) shows that the higher E/N better focuses ions to the central axis of the reactor and increases the sensitivity. This may explain the uptick in sensitivities when E/N increases from 80 to 90 Td, which is not observed in the modeled $NH_4^+ \cdot H_2O$. Overall, the observed dependence of sensitivities on E/N is a superposition of at least three effects, focusing effects and the extent of declustering of both reagent ions and product ions.

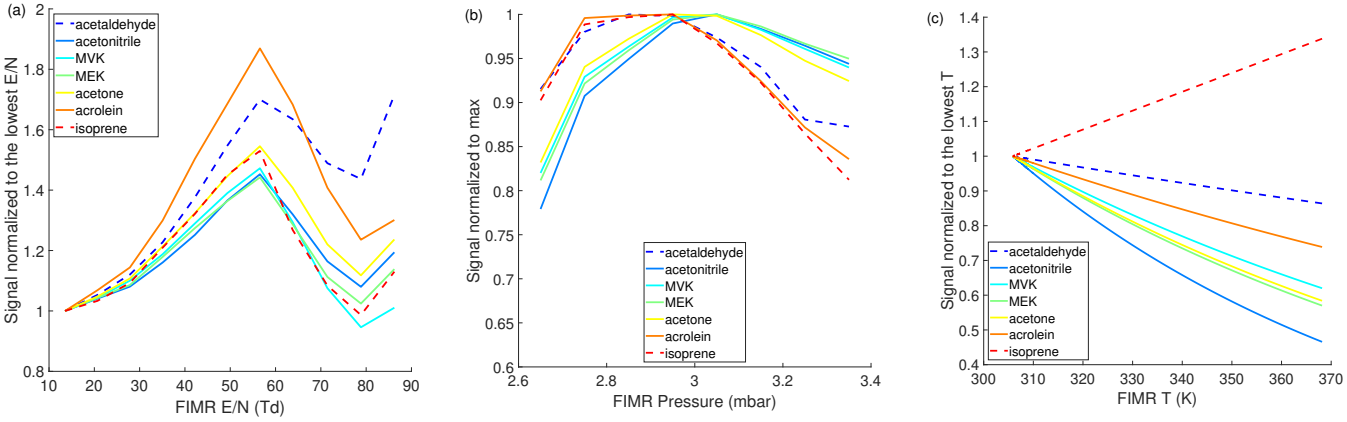

Figure 2. Dependence of instrument sensitivities of representative species on FIMR conditions (a) E/N; (b) P; (c) T. The range of E/N in panel (a) is obtained by varying the drift voltage while maintaining the P and T at 3 mbar and 313 K, respectively. Analytes with sensitivities lower than 50 cps $ppbv^{-1}$ are shown in dashed lines. The parent ion $NH_4^+ \cdot A$ is used to quantify the sensitivity.

The effects of FIMR pressure on sensitivities are shown in Figure 2b. The sensitivities exhibit a non-monotonic dependence on FIMR pressure, in a similar manner as the reagent ion $NH_4^+ \cdot H_2O$ does (Figure 1b), suggesting the pressure-dependent sensitivities are related to the pressure-dependent distribution of reagent ions. In addition, higher pressure increases the number density of analyte molecules in the FIMR, which tends to increase the sensitivity. However, this effect is smaller than the effect of changing reagent ion on sensitivities, as Figure 2b shows that the sensitivities decrease with increasing pressure beyond 3 mbar.

The effects of FIMR temperature on sensitivities are shown in Figure 2c. Among the seven compounds tested here, the sensitivities of six oxygenated compounds exhibit a negative dependence on the temperature between 310 and 370 K. The reduced VOC, isoprene, exhibits a positive dependence. Similar to isoprene, α-pinene sensitivity also increases with temperature in the 303 - 350 K window as recently reported in Khare et al. (2022). Here we examine the opposite trends of temperature-

dependent sensitivity between acetone and α-pinene, because their NH_4^+ affinities are available in the literature (Supplement S4). α-pinene has a NH_4^+ affinity smaller than that of H_2O (i.e., 75 vs 86 kJ mol^{-1} from Canaval et al. (2019)), resulting in the ligand-switching reaction between α-pinene and $NH_4^+ \cdot H_2O$ being endothermic. Therefore, the reaction is promoted under higher temperature, which enhances the sensitivity. In contrast, the ligand-switching reaction between acetone and $NH_4^+ \cdot H_2O$ is exothermic, because acetone has a larger NH_4^+ affinity than H_2O (i.e., 110 vs 86 kJ mol^{-1} from Canaval et al. (2019)). For exothermic reactions (ΔH is negative), higher temperature leads to smaller K_{eq} (Eqn. 8), smaller $k_{forward}/k_{reverse}$ ratio, and hence lower sensitivity. To better understand the temperature-dependent sensitivities, we add the reversible reactions of acetone and α-pinene with $NH_4^+ \cdot H_2O$ to the kinetic model depicted in Figure S4 and simulate the dependence of their sensitivities on temperature. As shown in Figure S6, the model can reproduce the observed dependence of their sensitivities on temperature. The NH_4^+ affinity of isoprene is not available, but it is expected to be even smaller than α-pinene, given that the isoprene sensitivity is 10 times smaller than that of α-pinene. Thus, the reaction between isoprene and $NH_4^+ \cdot H_2O$ is likely also endothermic, causing the increasing sensitivity with higher temperature as shown in Figure 2c.

The effects of NH_3/H_2O ratio on sensitivities are experimentally tested by simultaneously varying the flow rates of NH_3 and H_2O, while keeping the total flow rate constant. Because the NH_3 flow is a mixture of NH_3 and H_2O, the accurate flow rate of NH_3 is unknown. To approximate the NH_3/H_2O ratio, we use the observed ratio of $NH_4^+ \cdot H_2O/H_3O^+ \cdot H_2O$ and $NH_4^+ \cdot NH_3/NH_4^+ \cdot H_2O$, because these three ions have similar transmission efficiency and their relative abundance directly depends on the NH_3/H_2O ratio. Figure 3 shows the dependence of sensitivities of nearly 50 analytes on the $NH_4^+ \cdot H_2O/H_3O^+ \cdot H_2O$. For the majority of compounds, their sensitivities initially increase with $NH_4^+ \cdot H_2O/H_3O^+ \cdot H_2O$ and then show a decreasing trend. This trend is caused by the fact that the initial increase in NH_3/H_2O favors the formation of $NH_4^+ \cdot H_2O$ and hence higher sensitivity, but high NH_3/H_2O produces more $NH_4^+ \cdot NH_3$ clusters, leading to reduced sensitivity (Figure 1e). Taking acetone as an example, its NH_4^+ affinity (110 kJ mol^{-1}) is higher than that of H_2O (86 kJ mol^{-1}), but close to that of NH_3 (108 kJ mol^{-1}). As a result, the ligand-switching reaction between acetone and $NH_4^+ \cdot NH_3$ is less favorable than that between acetone and $NH_4^+ \cdot H_2O$. The sensitivities of several compounds, including D5-siloxane, texanol, and several monoterpenes, exhibit a monotonic increase with $NH_4^+ \cdot H_2O/H_3O^+ \cdot H_2O$ ratio within the tested range, but will likely decrease at a higher $NH_4^+ \cdot H_2O/H_3O^+ \cdot H_2O$ ratio. The maximum sensitivity occurs at different $NH_4^+ \cdot H_2O/H_3O^+ \cdot H_2O$ ratios for different compounds, likely because they have different reactivities towards $NH_4^+ \cdot H_2O$ and $NH_4^+ \cdot NH_3$.

Unlike the other four factors (i.e., E/N, T, P, and χ_{H_2O}) which can be accurately controlled, the NH_3/H_2O ratio and the resultant $NH_4^+ \cdot H_2O/H_3O^+ \cdot H_2O$ ratio change over time owing to the aging effects within the solution that supplies NH_3. In the current approach to supply the chemical ionization gas, the NH_3/H_2O ratio is controlled by the combination of the concentration of ammonium hydroxide aqueous solution and flow rates from the water and ammonium hydroxide reservoirs. Because NH_3 is more volatile than H_2O, the concentration of the ammonium hydroxide water solution decrease over time, resulting in a decreasing trend of NH_3/H_2O over timescale of weeks. In addition, the temperature variation of the ammonium hydroxide water solution changes the partitioning of NH_3 and hence the NH_3/H_2O ratio. One approach to compensate for the NH_3 loss is to adjust the flow rate from the ammonium hydroxide reservoir to maintain a relatively constant $NH_4^+ \cdot H_2O/H_3O^+ \cdot H_2O$ ratio. Future studies exploring approaches to reliably supply chemical ionization gas are warranted. In summary, the instrument

sensitivities should be calibrated as a function of $NH_4^+ \cdot H_2O/H_3O^+ \cdot H_2O$ ratio. Then, the optimal $NH_4^+ \cdot H_2O/H_3O^+ \cdot H_2O$ range can be selected based on the analytes of interest.

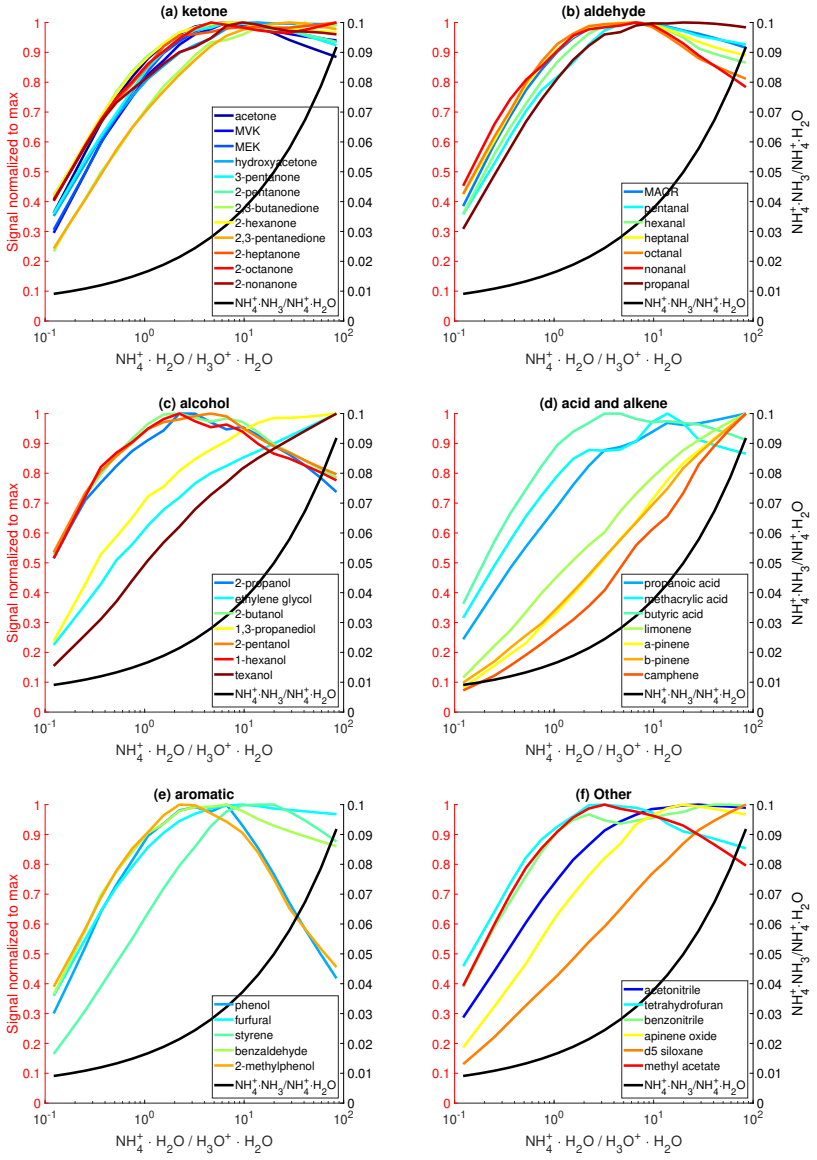

Figure 3. The effects of reagent ion distribution on sensitivities of various organic species. The sensitivity of each analyte is normalized to the corresponding maximum value. Only analytes with sensitivity larger than 50 cps $ppbv^{-1}$ are shown here.

The impacts of various FIMR conditions on instrument sensitivities are highly intertwined. The relationship between instrument sensitivity and individual FIMR condition shown in Figure 2 could change when other FIMR conditions change. The optimal FIMR conditions should be explored collectively and systematically. The optimal condition for our instrument is

FIMR drift voltage 55 Td, 3 mbar, 40°C, 1 sccm from 0.5% ammonium hydroxide aqueous solution, and 20 sccm water vapor. A temperature value that is slightly higher than ambient temperature is chosen for control purpose.

3.4 Product Distributions from the Ion-Molecule Reactions

The desired reagent ion is $NH_4^+ \cdot H_2O$ and the desired ion-molecule reaction is the ligand-switching reaction between $NH_4^+ \cdot H_2O$ and analyte A, which produces cluster $NH_4^+ \cdot A$ as the parent ion (Eqn. 5). However, the presence of several reagent ions in the FIMR and the declustering of $NH_4^+ \cdot A$ in the electric field induce a variety of reactions and causes complex product distributions. Besides the target parent ion $NH_4^+ \cdot A$, we observe the protonated product (AH^+), analyte clusters ($NH_4^+ \cdot H_2O \cdot A$, $H_3O^+ \cdot A$, and $H_3O^+ \cdot H_2O \cdot A$), and fragmentation products. The potential ion-molecule reactions and product ions can be generally expressed by reactions 11 and 12.

$$\begin{aligned} NH_4^+ \cdot (NH_3)_x \cdot (H_2O)_y + A &\rightarrow NH_4^+ \cdot A \ + \ xNH_3 \ + \ yH_2O \\ &\rightarrow NH_4^+ \cdot H_2O \cdot A \ + \ xNH_3 \ + \ (y-1)H_2O \\ &\rightarrow AH^+ \ + \ (x+1)NH_3 \ + \ yH_2O \\ &\rightarrow H_3O^+ \cdot A \ + \ (x+1)NH_3 \ + \ (y-1)H_2O \\ &\rightarrow H_3O^+ \cdot H_2O \cdot A \ + \ (x+1)NH_3 \ + \ (y-2)H_2O \\ &\rightarrow \text{fragments} \end{aligned} \tag{11}$$

$$\begin{aligned} H_3O^+ \cdot (H_2O)_n + A &\rightarrow H^+ \cdot (H_2O)_m \cdot A \ + \ (n-m+1)H_2O \\ &\rightarrow \text{fragments} \end{aligned} \tag{12}$$

Figure 4 shows the product distributions for all tested analytes, grouped by their chemical class. The analyte sensitivities are represented by the circle size in the figure. Among all classes, acids, ketones, and nitriles have the most desirable product distribution, in which the fraction of parent ion $NH_4^+ \cdot A$ in all product ions (denoted as $f_{NH_4^+ \cdot A}$) is more than 90%, with the exceptions of acetic acid. For 2-octanone and 2-nonanone, $NH_4^+ \cdot A$ is the sole product ion. For the alcohols, the product distribution is diverse. 2-propanol and 2-butanol have fragmentation products ($NH_4^+ \cdot A - 2H$), which account for ~5% of the total products, but the fragmentation mechanism is unclear. For the aldehydes, the $NH_4^+ \cdot A$ generally accounts for more than 80% of total product ions. The $f_{NH_4^+ \cdot A}$ tends to increase with larger molecules, for example, when comparing a homologous series of aldehydes (pentanal, hexanal, heptanal, octanal, and nonanal). Four monoterpenes studied here produce significant amount of protonated product (AH^+), which is comparable to that of $NH_4^+ \cdot A$. The causes of the product distributions of four monoterpenes are possibly explained by their proton affinity and NH_4^+ affinity. Three monoterpenes including α-pinene, β-pinene, and camphene have smaller NH_4^+ affinities than H_2O (Table S2). Thus, their ligand-switching reactions with $NH_4^+ \cdot H_2O$ are endothermic and the production of $NH_4^+ \cdot A$ is likely aided by the energetic collision energy imparted by the drift voltage. These three monoterpenes have higher proton affinity than NH_3 (Table S2), so that $NH_4^+ \cdot A$ can undergo internal proton transfer

to produce $AH^+ \cdot NH_3$, which breaks in the electric field and produces AH^+. In contrast to the above three monoterpenes, limonene has larger NH_4^+ affinity than H_2O and smaller proton affinity than NH_3 (Table S2). Thus, the ligand-switching reaction with $NH_4^+ \cdot H_2O$ is exothermic and the internal proton transfer reaction is thermodynamically unfavorable. For limonene, the $C_{10}H_{16}H^+$ is likely produced from the declustering of $NH_4^+ \cdot C_{10}H_{16}$ in the electric fields. The energy released from the exothermic reaction together with that imparted via the drift voltage could even break $NH_4^+ \cdot$ limonene into fragments $C_6H_9^+$, $C_7H_{11}^+$, and $C_6H_{12}N^+$. As a result, limonene produces ~20% of fragmentation products. For reduced aromatics (toluene, o-xylene, m-xylene, 1,2,4-TMB, and p-cymene), AH^+ is the dominant product and $NH_4^+ \cdot A$ is negligible. The product distributions of reduced aromatics are puzzling, because these analytes have lower proton affinity than NH_3. Since their sensitivities are < 2 cps $ppbv^{-1}$, it is not recommended to use $NH_4^+ \cdot H_2O$ to quantify reduced aromatics. Compared to reduced aromatics, oxygenated aromatics have higher sensitivities and larger values of $f_{NH_4^+ \cdot A}$. For example, benzaldehyde, 2-methylphenol, and furfural have $f_{NH_4^+ \cdot A}$ greater than 90%.

For a number of analytes in this study, the production of $NH_4^+ \cdot H_2O \cdot A$ is evident. This product complicates the interpretation of the mass spectra and introduces uncertainties in quantification, because the same ion is produced from an analyte (A) clustering with $NH_4^+ \cdot H_2O$ and an analyte with chemical formula $A+H_2O$ clustering with NH_4^+. For example, the ion $C_3H_{12}NO_2^+$ can be produced from either acetone (C_3H_6O) clustering with $NH_4^+ \cdot H_2O$ or 1,3-propanediol ($C_3H_8O_2$) clustering with NH_4^+. Cluster ions with $NH_4^+ \cdot NH_3$ are not observed for any compound. Overall, the product distribution is complicated and caution is required in quantification.

3.5 Constraining the Sensitivity

Because of a lack of calibration standards, the NH_4^+ CIMS sensitivities towards the majority of routinely detected multifunctional organic compounds in the atmosphere are not quantifiable. We attempt to constrain the sensitivity building upon the extensive calibration of organic compounds from various chemical classes in this study. The observed instrument sensitivity (S, cps $ppbv^{-1}$) is defined as the detected analyte signal (i.e., $[NH_4^+ \cdot A]$, cps) at a volume mixing ratio of 1 ppbv. Fundamentally, S depends on the product ion formation and the transmission efficiency of product ions, as expressed by Eqn. 13 (Lopez-Hilfiker et al., 2016), where the integral represents the formation of product ions via the ion-molecule reactions in the IMR, $f_{NH_4^+ \cdot A}$ represents the fraction of parent ion $NH_4^+ \cdot A$ in all product ions, and TE represents the transmission efficiency of parent ion, which is dependent on the mass-to-charge ($\frac{m}{Q}$) and the binding energy (B) of parent ion. In the integral, $[NH_4^+ \cdot H_2O]$ represents the $NH_4^+ \cdot H_2O$ concentration in the IMR, k and t represent the reaction rate constant and reaction time between reagent ion $NH_4^+ \cdot H_2O$ and analyte (A) in the IMR, respectively. Using this integral to represent the product ion formation is only valid when the ion-molecule reaction is in the kinetic-limited regime. In the thermodynamic regime, both forward and reverse ion-molecule reactions need to be considered.

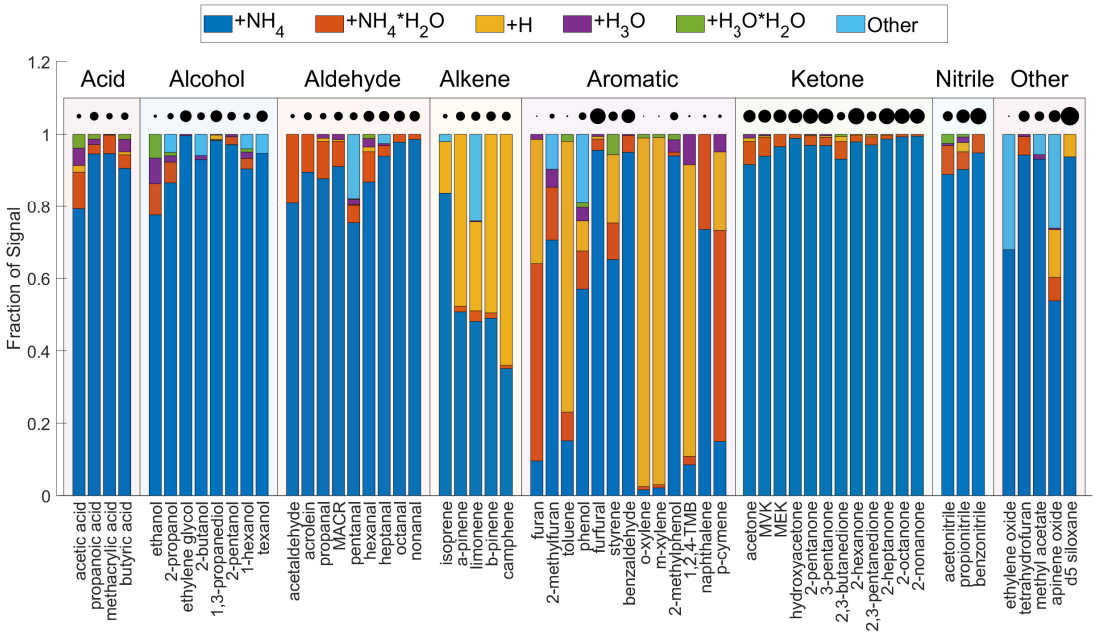

Figure 4. The product distributions of analytes in the NH_4^+ CIMS. The analytes are grouped by chemical class. Within each class, the analytes are sorted by increasing molecular weight. The distributions are obtained under the condition that the ratio of $NH_4^+ \cdot H_2O$ to $H_3O^+ \cdot H_2O$ is between 5 and 20. The product ion labeled "other" includes charge transfer products (e.g., $C_6H_6O^+$ for phenol), and fragmentation products (e.g., $C_5H_{12}N^+$ for pentanal). The product distribution of benzene is not shown because the signals of its product ions are too low to be reliably fitted. The circles are scaled to the square root of the analyte sensitivity.

$$S = \left(f_{NH_4^+ \cdot A} \times \int_0^t k \times [NH_4^+ \cdot H_2O]\, dt \right) \times \left(TE(\frac{m}{Q}, B) \right) \tag{13}$$

$$= \text{parent ion formation} \times \text{transmission efficiency}$$

$$TE(\frac{m}{Q}, B) = TE_{\frac{m}{Q}} \times TE_B \tag{14}$$

$$f(KE_{cm,50}) = TE_B = \frac{1}{\int_0^t [NH_4^+ \cdot H_2O]\, dt} \times \frac{S}{f_{NH_4^+ \cdot A} \times k \times TE_{\frac{m}{Q}}} = \frac{1}{C} S_{corr} \tag{15}$$

Under a constant instrumental condition, the $[NH_4^+ \cdot H_2O]$ and reaction time are fixed. The sensitivity of an analyte is determined by $f_{NH_4^+ \cdot A}$, k, and TE. Among these three factors, $f_{NH_4^+ \cdot A}$ and k are more uncertain than TE. The value of k for exothermic

ligand-switching reactions is close to the collisional limit (Adams et al., 2003), which can be calculated according to Su (1994) using the dipole moment and polarizability of the analyte (Table S3). $f_{NH_4^+ \cdot A}$ can be experimentally measured and it is close to 1 for multifunctional organic compounds, as discussed in Section 3.4. The TE, which represents the survival chance of ions through ion optics, is difficult to quantify. We assume the overall TE is represented by the product of $\frac{m}{Q}$-dependent TE (denoted as $TS_{\frac{m}{Q}}$) and binding energy-dependent TE (denoted as TE_B) (Eqn. 14). $TS_{\frac{m}{Q}}$ represents the transmission efficiency through BSQ, extraction region of the ToF, and other processes that are dependent on $\frac{m}{Q}$. $TS_{\frac{m}{Q}}$ is experimentally quantified as described in Section 2.2. TE_B accounts for the ion loss via collision-induced dissociation caused by energy imparted by electric fields. TE_B depends on the binding energy of the parent ion, as the parent ion with stronger bonds between analyte and NH_4^+ have a larger chance to survive the electric fields and hence a larger TE_B. The binding energy of $NH_4^+ \cdot A$ is experimentally probed from the voltage scanning tests and is represented by the kinetic energy of $NH_4^+ \cdot A$ in the center of mass (i.e., $KE_{cm,50}$) (Section 2.2). In this way, TE_B is related to a measurable parameter $KE_{cm,50}$. The mathematical relationship between TE_B and $KE_{cm,50}$, $TE_B = f(KE_{cm,50})$, is the final component to constrain the sensitivity.

We utilize the extensive calibration of 60 compounds from diverse chemical classes to derive the relationship between TE_B and $KE_{cm,50}$. By rearranging Eqns. 13 and 14, and representing $\int_0^t [NH_4^+ \cdot H_2O]\,dt$ as a constant C, TE_B can be expressed as Eqn. 15, where S_{corr} represents the sensitivity corrected for $f_{NH_4^+ \cdot A}$, k, and $TE_{\frac{m}{Q}}$. Using Eqn. 15, the relationship between TE_B and $KE_{cm,50}$ can be obtained through plotting S_{corr} against $KE_{cm,50}$. As shown in Figure 5, S_{corr} exhibits a positive dependence on $KE_{cm,50}$. The relationship between S_{corr} and $KE_{cm,50}$ of the majority of compounds can be reasonably described using a Hill Equation. Analytes with small $KE_{cm,50}$ (i.e., < 0.15 eV) have very low sensitivity, because of declustering of $NH_4^+ \cdot A$ in the electric fields. As $KE_{cm,50}$ increases, the sensitivity increases. This is because $NH_4^+ \cdot A$ with a stronger bond between A and NH_4^+ is more likely to survive the imparted energy from electric fields and hence more likely to be detected. When $KE_{cm,50}$ exceeds a threshold (i.e., 0.35 eV), $NH_4^+ \cdot A$ does not decluster in the electric field and it is detected with maximum S_{corr}. The maximum S_{corr} is constrained using 2-hexanone here, but calibrations of analytes with $KE_{cm,50}$ larger than 0.35 eV are warranted to constrain the maximum S_{corr}. Such analytes tend to be large oxygenated organic compounds with low volatility, making their calibrations challenging.

A similar relationship between S_{corr} and $KE_{cm,50}$ has been reported in Zaytsev et al. (2019), which used a NH_4^+ – PTR3 and explored the relationship between the sensitivity and $KE_{cm,50}$ for 16 compounds, 9 of which are ketones. Unlike this study, Zaytsev et al. (2019) did not normalize the sensitivity to the ion-molecule collision rate constant k. This is reasonable as the ion-molecule reaction time in NH_4^+ – PTR is $\sim$3 ms, about 15 times longer than that in our instrument. The long reaction time results in an equilibrium between cluster formation and fragmentation in the IMR for many analytes. In this thermodynamic regime, the product ion formation is proportional to the equilibrium constant of reaction 6 (Iyer et al., 2016; Robinson et al., 2022), so that normalizing the sensitivity in NH_4^+ – PTR3 by the equilibrium constant may improve the relationship between sensitivity and $KE_{cm,50}$ in Zaytsev et al. (2019).

In this study, the relationship between S_{corr} and $KE_{cm,50}$ is largely defined by monofunctional organic compounds, but we anticipate this relationship applies to organic compounds containing at least one functional group that binds strongly with NH_4^+, such as C=O, -OH, and nitrile. For example, five multifunctional compounds studied here (i.e., ethylene glycol, 1,3-

propanediol, hydroxyacetone, 2,3-butanedione, and 2,3-pentanedione) are well described by the fitted Hill equation. Because the fitted Hill equation does not apply to monocarboxylic acids, for reasons discussed later, the applicability of the relationship to multifunctional organic acids is uncertain and it warrants future investigation. Moreover, we compare several structural isomers with monofunctional group, including acetone vs propanal, MACR vs MVK, C5-C9 mono-aldehyde vs mono-ketones. Despite the difference in S_{corr} between isomers, their S_{corr} and $KE_{cm,50}$ follow the same relationship.

The relationship between S_{corr} and $KE_{cm,50}$ depicted in Figure 5 provides an effective approach to estimate the sensitivity of the NH_4^+ CIMS towards a suite of oxygenated organic compounds. The $KE_{cm,50}$ can be calculated from the voltage scan tests. $TE_{\frac{m}{Q}}$ can be experimentally quantified following the procedure in Section 2.2. $f_{NH_4^+ \cdot A}$ is unknown, but it is close to 1 for multifunctional organic compounds, as discussed in Section 3.4. The k is also unknown, but it can be either calculated (Su, 1994) or reasonably estimated based on the molecular mass, elemental composition, and functional group (Sekimoto et al., 2017). k is generally on the order of 10^{-9} cm^3 $molecule^{-1}$ s^{-1} (Figure S7). Finally, based on above-mentioned four parameters, the sensitivity can be estimated.

The observed relationship between S_{corr} and $KE_{cm,50}$ in Figure 5 has limitations. First, it is only applicable to analytes of which the ligand-switching reaction with $NH_4^+ \cdot H_2O$ is exothermic. This arises from approximating the ion-molecule reaction rate constant (k) in S_{corr} using the collisional limiting rate constant. This approximation is not valid for endothermic reactions, which occur at a slower rate. This likely explains why several compounds, including monocarboxylic acids, some monoterpenes, reduced aromatics, isoprene, and 2-methylfuran, are outliers in Figure 5. For example, the NH_4^+ affinity of acetic acid is estimated to be lower than H_2O (Section S5). Two monoterpenes, limonene and α-pinene, do not follow the fitted line, but the behaviors of monoterpenes are more complicated. The calculated NH_4^+ affinities of β-pinene and camphene are smaller than that of H_2O (Table S2), causing their ligand-switching reactions to be endothermic, but they fall on the fitted Hill equation. In contrast, limonene has larger NH_4^+ affinity than H_2O, but it is lower than the fitted line. The reason for such different behavior is unknown, but might be related to their structural difference. For example, β-pinene and camphene have an external C=C bond connected to the six-member ring, but α-pinene and limonene do not. Another limitation is that $KE_{cm,50}$, which is calculated from ΔV_{50} based on voltage scan, may not be a proper proxy of NH_4^+ affinity for some analytes. For example, α-pinene has similar NH_4^+ affinity as β-pinene and camphene (Canaval et al., 2019), but the voltage scan test shows that α-pinene has a larger $KE_{cm,50}$ than the other two (Figure 5). Another exception is that isoprene and 2-methylfuran are expected to have small NH_4^+ affinity, considering their low sensitivities, but their $KE_{cm,50}$ is the highest among all analytes studied here. Similar "false positive" behavior (i.e., large $KE_{cm,50}$ or binding energy, but low sensitivity) is also observed in the I^- CIMS (Iyer et al., 2016). We suspect the voltage scanning affects not only the collisional energy of the $NH_4^+ \cdot A$, but also the ion-molecule chemistry or ion transmission via some unknown mechanisms. In the voltage scan, the FIMR front voltage is increased simultaneously with FIMR back voltage to keep the upstream voltage gradient constant. It is generally assumed that the absolute voltages do not affect the ion-molecule chemistry and transmission, as long as the voltage gradient is constant, but this assumption may not be valid. For example, in the voltage scan, we observe that the signal of reagent ion becomes noisy when the FIMR front voltage (450 V) is close to the ion source voltage (440 V), suggesting that the FIMR front voltage affects the ion transmission from the ion source into the FIMR.

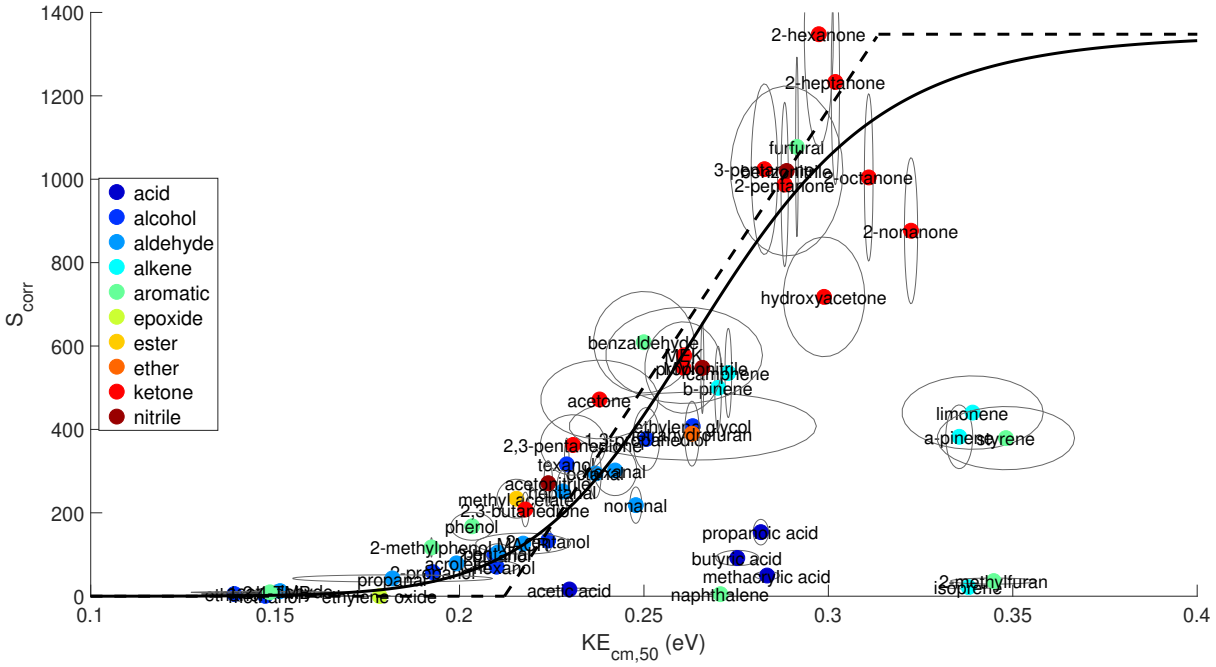

Figure 5. Relationship between S_{corr} and $KE_{cm,50}$. S_{corr} represents the sensitivity (cps ppbv^{-1}) corrected for the fraction of parent ion in all product ions ($f_{NH_4^+ \cdot A}$), m/Q-dependent transmission efficiency ($TE_{m/Q}$), and the ion-molecule reaction rate constant (k, 10^{-9} cm^3 molecule^{-1}), as defined in Eqn. 15. The solid line represents a fitting of analytes using a Hill Equation. $S_{corr} = 1350/(1+(0.267/KE_{cm})^{11})$. The dashed line represents a linear fitting for analytes with KE_{cm} between 0.2 and 0.3 eV in a similar fashion done in Zaytsev et al. (2019). Organic acids, naphthalene, isoprene, 2-methyl furan, limonene, α-pinene, and styrene are excluded from both fittings. The ellipses represent the uncertainty range.

3.6 Comparison of Sensitivities between Instruments

In this section, we compare the sensitivities of our NH_4^+ CIMS (denoted as NOAA NH_4^+ CIMS) to two other NH_4^+ CIMS and a H_3O^+ CIMS. The other two NH_4^+ CIMS include a PTR3 instrument with a different IMR design from our Vocus (Zaytsev et al., 2019) (denoted as PTR3 NH_4^+ CIMS) and a Vocus instrument with the same IMR design as ours but operated under different conditions (Khare et al., 2022) (denoted as Khare NH_4^+ CIMS). The H_3O^+ CIMS is from our lab (denoted NOAA H_3O^+ CIMS), which replaced the traditional drift tube with the same FIMR as used in the NH_4^+ CIMS. The NOAA H_3O^+ CIMS was calibrated along with the NH_4^+ CIMS using the same calibration methods. The sensitivities of PTR3 NH_4^+ CIMS and Khare NH_4^+ CIMS are obtained from the corresponding references.

Figure 6 shows the sensitivity ratio of a selected instrument (S_i) to the NOAA NH_4^+ CIMS ($S_{NH_4^+\,CIMS}$) for a number of analytes grouped by their chemical class. Khare NH_4^+ CIMS used the same ion source and IMR as NOAA NH_4^+ CIMS, but the sensitivities are generally lower than NOAA NH_4^+ CIMS by a factor of 5. In particular, the ethylene glycol sensitivity is lower by a factor of 100. The lower sensitivity in Khare et al. (2022) is likely because they used a higher NH_3/H_2O ratio than

this study. Khare et al. (2022) used 1 sccm vapor from a 1% ammonium hydroxide solution, while this study used 1 sccm vapor from a 0.5% solution. As discussed in Section 3.2, larger NH_3/H_2O ratio leads to a larger fraction of $NH_4^+ \cdot NH_3$ in the total reagent ions and hence reduced sensitivity for most analytes (Figure 3). The sensitivities in Khare et al. (2022) can be reproduced in NOAA NH_4^+ CIMS by using a larger NH_3 flow rate. The comparison between NOAA NH_4^+ CIMS and Khare NH_4^+ CIMS further emphasizes the importance of FIMR conditions on the instrument performance.

The sensitivity ratio of NOAA H_3O^+ CIMS to NOAA NH_4^+ CIMS does spans a wide range from 1 to 10^4. In general, the sensitivity ratio anti-correlates with the sensitivity of NOAA NH_4^+ CIMS within each chemical class. This trend is the most evident for aromatics. For example, for reduced aromatics, of which the sensitivities are smaller than 2 cps $ppbv^{-1}$ in the NOAA NH_4^+ CIMS, their sensitivities are 10^3 higher in the NOAA H_3O^+ CIMS. However, for oxygenated aromatics, such as benzaldehyde and furfural, of which the sensitivities are on the order of 10^3 cps $ppbv^{-1}$ in NOAA NH_4^+ CIMS, two instruments have similar sensitivities. Therefore, H_3O^+ chemistry is more suitable to quantify reduced VOCs and small oxygenated VOCs (e.g., acetic acid, methanol, acetaldehyde) than $NH_4^+ \cdot H_2O$ chemistry. $NH_4^+ \cdot H_2O$ chemistry is better for quantifying larger oxygenated VOCs, because it causes less fragmentation than the H_3O^+ chemistry (Pagonis et al., 2019; Yuan et al., 2017; Sekimoto et al., 2017), which simplifies the interpretation of the mass spectra.

Using the same $NH_4^+ \cdot H_2O$ chemistry, the PTR3 sensitivities are overall 20 times higher than those of NOAA NH_4^+ CIMS. This difference is mainly due to different designs of the IMR and ion source. The PTR3 utilized a tripole electrode as IMR (Breitenlechner et al., 2017). This design enables the IMR to be operated at 60 mbar and 3 ms reaction time (Zaytsev et al., 2019), which are much higher than 3 mbar and 0.2 ms in NOAA NH_4^+ CIMS, and leads to enhanced sensitivities. The NOAA NH_4^+ CIMS utilizes a low pressure discharge ion source, which generates more ions than the corona discharge ion source in the PTR3. This compensates the effects of the lower IMR pressure and short reaction reaction on sensitivity to some extent. The combined influences of ion source, IMR pressure, and reaction time result in the difference in sensitivities between NOAA NH_4^+ CIMS and PTR3 NH_4^+ CIMS. Despite of lower sensitivities, one advantage of the NOAA NH_4^+ CIMS is that its sensitivities have much smaller dependence on the sample relative humidity that the PTR3 NH_4^+ CIMS does (Zaytsev et al., 2019).

4 Field Deployment

The NH_4^+ CIMS was deployed during the RECAP campaign in Pasadena, California in August-September, 2021. Measurements presented in this section were made from August 10th to 19th when the instrument continuously sampled gas phase.

4.1 Measurement Capability

Figure S8 uses a mass defect plot to illustrate the measurement capability of NH_4^+ CIMS. In the RECAP campaign, a total of 288 ions have signals above the detection limit. Half of the ions have the formula $C_xH_yN_1O_z$ (reagent ion included in the formula). These ions mostly represent the non-nitrogen-containing oxygenated organics cluster with NH_4^+ or $NH_4^+ \cdot H_2O$. 70 ions have the formula $C_xH_yN_2O_z$, which likely represent nitrogen-containing compounds. This assignment is supported by the

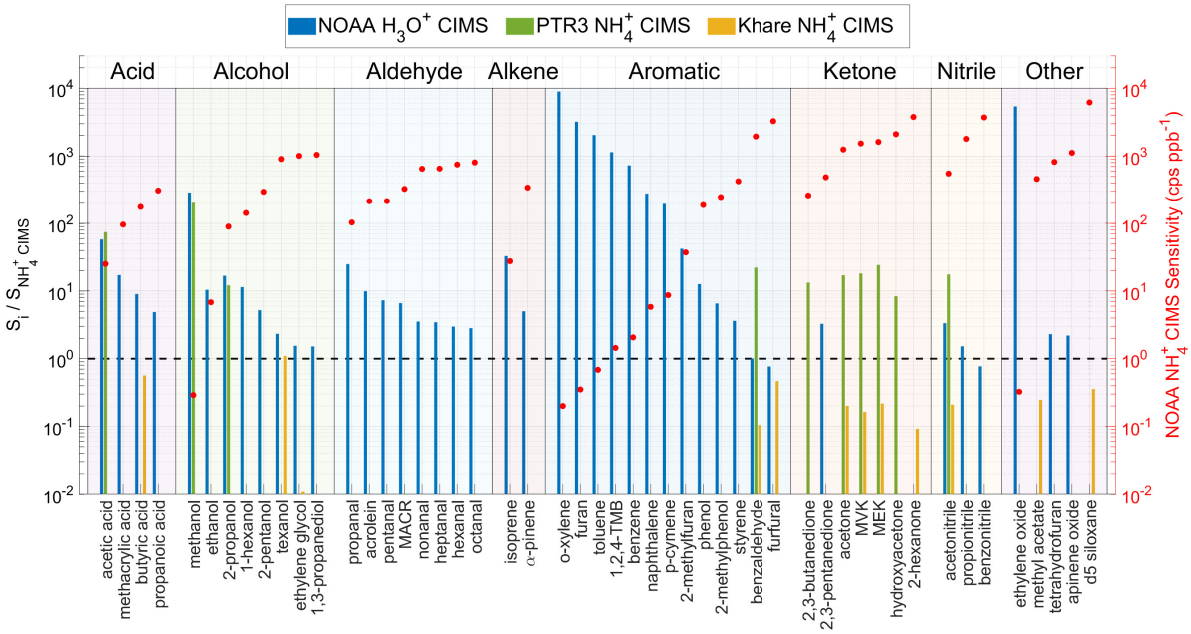

Figure 6. The sensitivity ratio of a selected instrument (S_i) to the NOAA NH_4^+ CIMS ($S_{NH_4^+ CIMS}$). The selected instrument i includes PTR3 NH_4^+ CIMS, Khare NH_4^+ CIMS, and NOAA H_3O^+ CIMS. The analytes are grouped by their chemical class. Within each chemical class, the analytes are sorted by their sensitivity.

analysis of product distribution (Section 3.4), which shows the product ion contains at most one nitrogen from the reagent ion. 40 out of 288 ions have the formula $C_xH_yO_z$, which likely represent analytes clustering with $H^+ \cdot (H_2O)_n$ (n=0,1,2).

4.2 Instrument Intercomparison

The co-located instruments in the RECAP campaign enable the evaluation of the field performance of NH_4^+ CIMS. In this section, we compare the measurements of several important atmospheric species from different chemical classes by three NOAA mass spectrometers (i.e., NH_4^+ CIMS, H_3O^+ CIMS, GC-MS) and the Caltech CF_3O^- CIMS. For compounds that are commercially available, we calibrate the instrumental sensitivity and compare the mixing ratio. For multifunctional oxygenated organics that do not have calibration standards, raw signals are compared. If multiple isomers exist for a parent ion and if these isomers are quantified by GC-MS, we apply the GC-MS resolved isomer ratio and the sensitivities of individual isomers to convert the raw cps of the parent ion to the summed mixing ratio of all isomers for NH_4^+ CIMS (Supplement S6).

To account for instrument variability, the ion signals are typically normalized to the changing reagent ion signals. However, previous studies using Vocus in H_3O^+ and $NH_4^+ \cdot H_2O$ chemistry did not normalize the signals to reagent ions (Krechmer et al., 2018; Khare et al., 2022), because the BSQ serves as a high-pass band filter and substantially reduces the signal intensity of reagent ions. In this study, we find that without normalization, the comparisons between NH_4^+ CIMS and GC-MS exhibit

significant difference between day and night (Figure S9a and b), which is consistent with the diurnal trend of reagent ion $NH_4^+ \cdot H_2O$ (Figure S9c). Normalization to the reagent ion signal largely eliminates this difference. In light of this observation, we normalize the ion signals to that of $NH_4^+ \cdot H_2O$ and then apply the normalized sensitivity to convert the signal (ncps) to mixing ratio (ppbv).

4.2.1 Reduced VOCs

We compare the measurements of isoprene and monoterpenes between NH_4^+ CIMS, H_3O^+ CIMS, and GC-MS (Figure 7a and b). NH_4^+ CIMS has a relatively low sensitivity towards isoprene (i.e., 28 cps $ppbv^{-1}$), but the high mass resolution of the instrument enables a clear separation of isoprene (detected as $NH_4^+ \cdot C_5H_8$) from other isobars. Overall, isoprene measured by NH_4^+ CIMS is ∼20% higher than H_3O^+ CIMS and GC-MS (Figure S10). At night, both NH_4^+ CIMS and H_3O^+ CIMS observe significantly higher isoprene concentration than GC-MS does (Figure 7a). This is likely because isoprene measured by NH_4^+ CIMS and H_3O^+ CIMS has interference from fragments of other species. We found that several aldehydes, including octanal and nonanal, fragment in the H_3O^+ CIMS and produce $C_5H_8H^+$. Correcting such interference results in lower isoprene concentration measured by the H_3O^+ CIMS, particularly at night, and better agreement between H_3O^+ CIMS and GC-MS (Figure 7a). Similarly, pentanal in the NH_4^+ CIMS produces $NH_4^+ \cdot C_5H_8$, which is the parent ion of isoprene. Because the isoprene sensitivity in NH_4^+ CIMS is so low, the production of $NH_4^+ \cdot C_5H_8$ from an analyte with high sensitivity would lead to large interference in isoprene concentration. Thus, NH_4^+ CIMS is not recommended for quantifying isoprene.

For monoterpenes, GC-MS shows that α-pinene and β-pinene are the dominant monoterpene isomers at the sampling site. The ratio of α-pinene and β-pinene measured by GC-MS is used to convert $NH_4^+ \cdot C_{10}H_{16}$ signal measured by NH_4^+ CIMS to the mixing ratio of total monoterpenes (Supplement S6). Three instruments show a large difference in measuring monoterpenes (Figure 7b). The correlation between H_3O^+ CIMS and NH_4^+ CIMS is strong, but H_3O^+ CIMS observes three times more monoterpenes than NH_4^+ CIMS (Figure S10b). NH_4^+ CIMS and GC-MS agree well at night, but NH_4^+ CIMS detects more monoterpenes in the afternoon than GC-MS does (Figure 7b). The monoterpenes concentrations measured by both the NH_4^+ CIMS and the H_3O^+ CIMS are very spiky in the afternoon and the afternoon peak in the diurnal trend coincides with that of isoprene (Figure S11). Both observations suggest that the monoterpenes are primary emissions from a local source, which is likely the trees a few meters away from the sampling site. The difference between three measurements may be related to fragmentation interference on the monoterpene signals measured by NH_4^+ CIMS (i.e., $NH_4^+ \cdot C_{10}H_{16}$) and H_3O^+ CIMS ($C_{10}H_{17}^+$). It is also possible that there are shorter-lived monoterpene isomers, other than α-pinene and β-pinene, which are not reported by the GC-MS, leading to the absence of an afternoon peak of monoterpenes in GC-MS.

4.2.2 Carbonyls

Figure 7c shows the time series of acetone measured by NH_4^+ CIMS, H_3O^+ CIMS, and GC-MS. In NH_4^+ CIMS, we attribute the $NH_4^+ \cdot C_3H_6O$ solely to acetone and ignore the contribution from its structural isomer propanal, because GC-MS shows propanal concentration is much lower than acetone and because the NH_4^+ CIMS sensitivity towards acetone is 10 times larger than propanal (1247 vs 103 cps $ppbv^{-1}$). Acetone concentrations measured by the three instruments agree within 15%, which

is within the combined calibration uncertainties. Similar to acetone, the MEK measurement agrees between NH_4^+ CIMS and GC-MS within 10% and an r^2 of 0.93 (Figure 7d).

For MACR+MVK, three instruments agree well in the day, but NH_4^+ CIMS and H_3O^+ CIMS observe higher concentration of MACR+MVK at night than GC-MS does (Figure 7e). We suspect the nighttime signal measured by NH_4^+ CIMS and H_3O^+ CIMS is due to 2-butenal and 3-butenal from cooking emissions.

4.2.3 Hydroxy nitrates

As shown in Figure S8, NH_4^+ CIMS detects a number of organic nitrates. Due to a lack of calibration standards, the sensitivities of organic nitrates in the NH_4^+ CIMS have not been quantified. Here, we explore the measurement capability of the NH_4^+ CIMS by comparing to three organic nitrates (i.e., $C_4H_7NO_5$, $C_5H_9NO_4$, and $C_5H_7NO_4$) measured by the CF_3O^- CIMS which has been calibrated (Lee et al., 2014b; Nguyen et al., 2014). All three organic nitrates are detected as adducts with the respective reagent ions in both instruments.

$C_4H_7NO_5$ matches the formula of hydroxynitrates produced from the oxidation of MACR, MVK, and first-generation organic nitrates from isoprene oxidation. The NH_4^+ CIMS and CF_3O^- CIMS show a correlation with an r^2 value of 0.91 (Figure 8a and S12a). $C_4H_7NO_5$ corresponds to at least two structural isomers, both of which have three functional groups (-OH, -C=O, and -ONO_2). The strong correlation between two instruments could be due to a dominance of a single isomer or similar sensitivities towards both isomers in each instrument.

$C_5H_9NO_4$ has been attributed to isoprene hydroxy nitrates (IHNs) in the literature (Lee et al., 2014b; Xiong et al., 2015; Nguyen et al., 2015; Lee et al., 2016; Teng et al., 2017; Vasquez et al., 2020). The correlation coefficient r^2 between the two instruments is 0.63 (Figure S12b). The $C_5H_9NO_4$ measured by CF_3O^- CIMS is close to zero at night (Figure 8b), consistent with previous isomer-resolved measurements of IHNs by the CF_3O^- CIMS coupled to a GC front end at the same site in 2017 (Vasquez et al., 2020). In contrast, the $C_5H_9NO_4$ measured by NH_4^+ CIMS is persistently high throughout the night. We hypothesize that the $C_5H_9NO_4$ signal measured by the NH_4^+ CIMS has a large contribution from nitrooxy ketones, which are produced from the oxidation of pentenes by nitrate radicals (Figure S13). Based on the laboratory characterization, $NH_4^+ \cdot H_2O$ is more sensitive to ketones than alcohols (Table 1 and Figure 5). Thus, it is possible that nitrooxy ketones have a much higher sensitivity than isoprene hydroxy nitrates in the NH_4^+ CIMS. This leads to the observed $C_5H_9NO_4$ signal in the NH_4^+ CIMS largely arising from nitrooxy ketones, even though their concentrations are much smaller than isoprene hydroxy nitrates. In contrast, the CF_3O^- CIMS likely has similar sensitivity towards both classes of chemicals (Lee et al., 2014b). Further, the nighttime signal of $C_5H_9NO_4$ measured by the NH_4^+ CIMS is consistent with the observation that pentene concentrations are higher at night than in the day (Figure S14).

$C_5H_7NO_4$ matches the formula of isoprene carbonyl nitrate, produced from isoprene oxidation by nitrate radicals followed by $RO_2 + RO_2$ reaction (Schwantes et al., 2015). Consistent with this product identification, the measurements of $C_5H_7NO_4$ by both NH_4^+ CIMS and CF_3O^- CIMS peak at night (Figure 8d). The correlation r^2 between NH_4^+ CIMS and CF_3O^- CIMS is 0.67 (Figure S12d).

5 Conclusions

In this study, we describe the development and deployment of a CIMS using $NH_4^+ \cdot H_2O$ as reagent ion. $NH_4^+ \cdot H_2O$ is a highly versatile reagent ion for measurements of a wide range of oxygenated organic compounds. The instrument sensitivities and product distributions are strongly dependent on the instrument conditions, including FIMR reduced electric field, temperature, pressure, the H_2O mixing ratio, and the ratio of NH_3 to H_2O. These conditions should be carefully selected to ensure $NH_4^+ \cdot H_2O$ as the predominant reagent ion and to optimize sensitivities. For example, a comparison between this study and another study using the same instrument but under different FIMR conditions shows that the instrument sensitivity can differ by a factor of 5. Besides the desired reagent ion $NH_4^+ \cdot H_2O$, several other reagent ions exist in the FIMR even at the optimal condition, which complicates the ion-molecule chemistry and the product distribution. The cluster ion $NH_4^+ \cdot A$ is the predominant product ion for acids, ketones, nitriles, and multifunctional oxygenated compounds. More diverse products, including protonated ion AH^+ and fragmentation ions, are observed for small alcohols, biogenic VOCs, and reduced aromatics.

For monofunctional analytes, the $NH_4^+ \cdot H_2O$ chemistry exhibits high sensitivity (i.e., > 1000 cps $ppbv^{-1}$) towards ketones, moderate sensitivity (i.e., between 100 and 1000 cps $ppbv^{-1}$) towards aldehdyes, alcohols, organic acids, and monoterpenes, low sensitivity (i.e., between 10 and 100 cps $ppbv^{-1}$) towards isoprene and C1 and C2 organics, and negligible sensitivity (i.e., < 10 cps $ppbv^{-1}$) towards reduced aromatics. The sensitivity of the NH_4^+ CIMS towards organic nitrates and highly oxygenated compounds requires further investigation. Overall, the NH_4^+ CIMS is complementary to existing chemical ionization schemes. Comparing to two commonly used reagent ions H_3O^+ and I^-, $NH_4^+ \cdot H_2O$ is more suitable to quantify moderately oxygenated compounds with one or two functional groups (i.e., C=O, -OH, and nitrile). These types of compounds have relatively low sensitivity in I^- CIMS (Lee et al., 2014a). H_3O^+ and $NH_4^+ \cdot H_2O$ show similar sensitivity towards the moderately oxygenated compounds, and one advantage of $NH_4^+ \cdot H_2O$ chemistry is that it causes less fragmentation than H_3O^+ chemistry (Pagonis et al., 2019), which simplifies the interpretation of the mass spectra. Moreover, we reveal a strong relationship between instrumental sensitivity and the binding energy of the analyte-NH_4^+ cluster, which can be estimated using voltage scanning tests. This offers the possibility to constrain the sensitivity of analytes for which no calibration standards exist. Caution is required when applying this method, because the observed relationship is only applicable to analytes of which the ligand-switching reaction with $NH_4^+ \cdot H_2O$ is exothermic and because the measured $KE_{cm,50}$ may not be a proper proxy of NH_4^+ affinity for some analytes. The combination of experimental constraints and theoretical calculation of analyte thermodynamic properties could potentially provide more accurate estimate of analyte sensitivities.

The field performance of the NH_4^+ CIMS is evaluated based on comparisons with three co-located mass spectrometers in the RECAP campaign during a 10-day period. NH_4^+ CIMS and GC-MS show reasonable agreement in measuring carbonyls (i.e., acetone, MEK, MACR+MVK), but not in isoprene and monoterpenes. Isoprene measured by the NH_4^+ CIMS has fragmentation interference. The difference in monoterpene measurements is possibly because of fragmentation interference in the NH_4^+ CIMS or some monoterpene isomers are not reported by the GC-MS. Future studies are needed to understand the difference. A number of nitrogen-containing species are detected by the NH_4^+ CIMS and three representative ones are compared to CF_3O^- CIMS. Strong correlations are observed for $C_4H_7NO_5$ (likely oxidation products of MACR, MVK, and first-generation organic

nitrates from isoprene oxidation), but not for $C_5H_9NO_4$ (including isoprene hydroxy nitrates and nitrooxy ketones from pentene oxidation). The difference in $C_5H_9NO_4$ measurements is likely because NH_4^+ CIMS and CF_3O^- CIMS have vastly different sensitivities towards different structural isomers. Such comparisons illustrate different measurement capabilities of different reagent ions. It is imperative to understand the isomer-specific sensitivity of instrument in order to obtain a complete and unbiased understanding of the atmospheric composition.

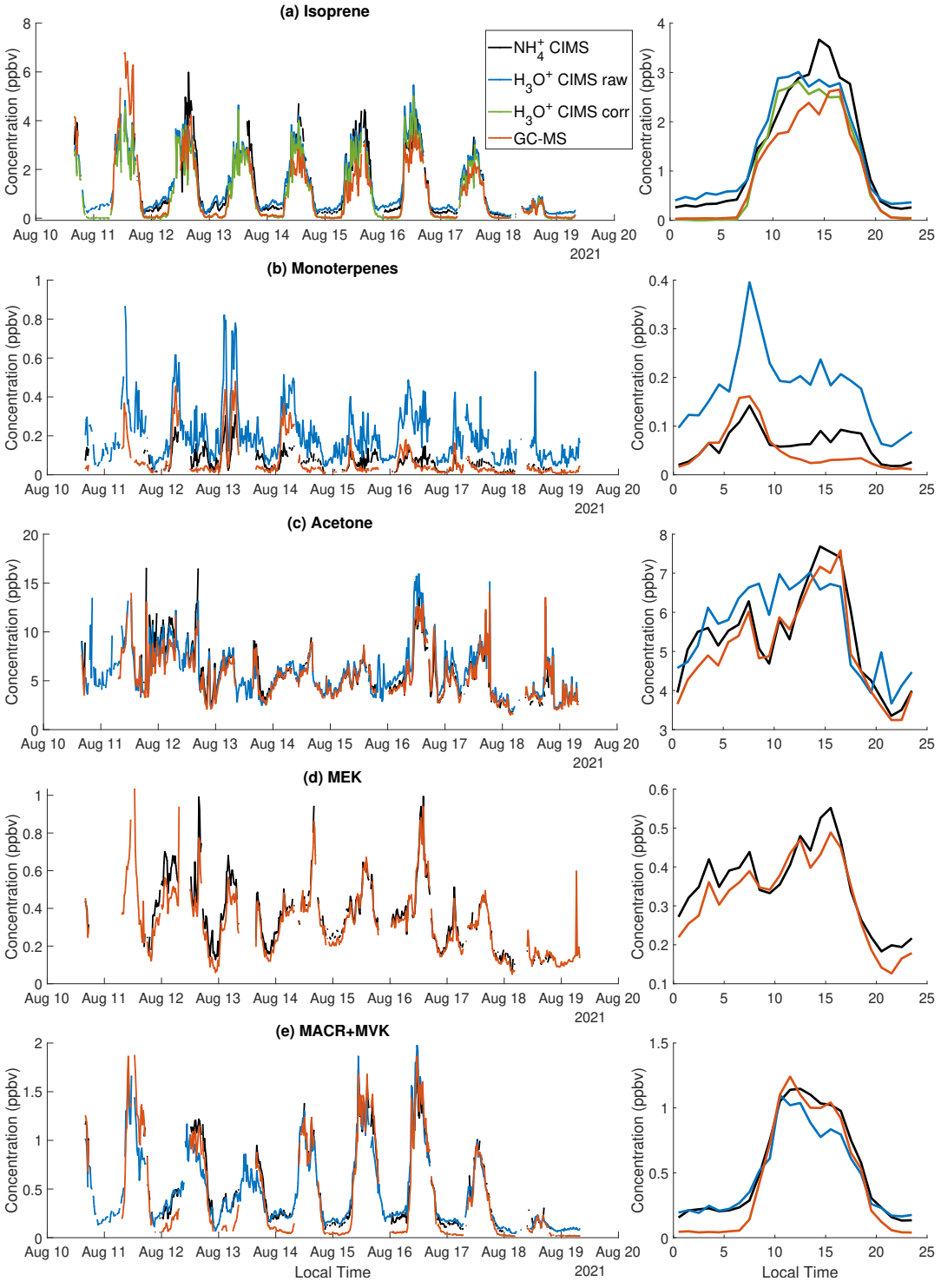

Figure 7. The time series and diurnal trend of selected species measured by NH_4^+ CIMS, H_3O^+ CIMS, and GC-MS. (a) Isoprene; (b) Monoterpenes; (c) Acetone; (d) Methyl Ethyl Ketone (MEK); (e) Methacrolein (MACR) + Methyl Vinyl Ketone (MVK). In panel (a), H_3O^+ CIMS corr represents the isoprene measurement by the H_3O^+ CIMS after correcting the interference from octanal and nonanal (Supplement S6). In panel (d), MEK measured by the NOAA H_3O^+ CIMS is not included because its peak fitting ($C_4H_9O^+$) is degraded by the nearby large signal of $H_9O_4^+$.

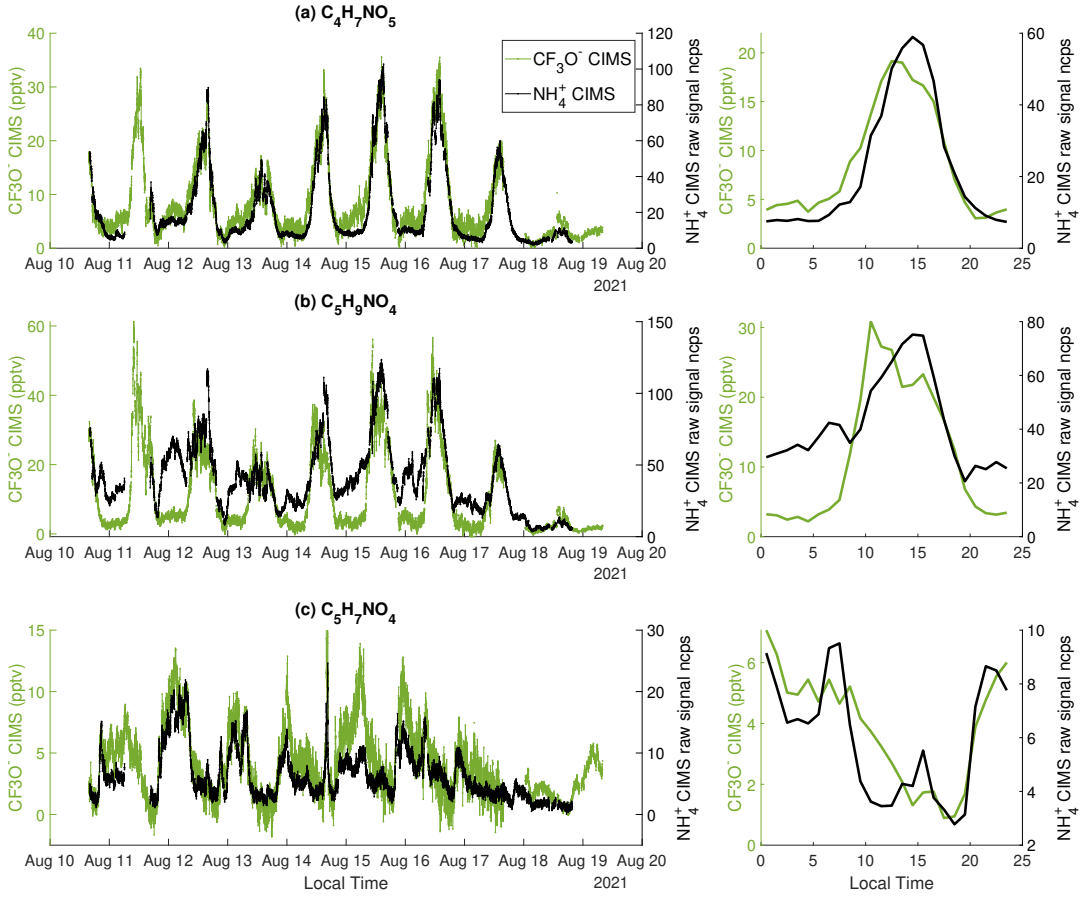

Figure 8. The time series and diurnal trend of three nitrogen-containing species measured by NH_4^+ CIMS and CF_3O^- CIMS. (a) $C_4H_7NO_5$; (b) $C_5H_9NO_4$; (c) $C_5H_7NO_4$. Because of a lack of calibration standards, the raw signals (ncps) of NH_4^+ CIMS are shown.

Data availability. Data from the RECAP campaign are available to the general public at
https://csl.noaa.gov/groups/csl7/measurements/2021sunvex/GroundLA/DataDownload/

Author contributions. LX and CW designed the research, LX operated the NH_4^+ CIMS, MMC and CES operated the H_3O^+ CIMS, JBG and AL operated the GC-MS, JDC and POW operated the CF_3O^- CIMS, MAR, JAN, PRV, GAN, MMC, CES, and SSB provided critical support and comments in NH_4^+ CIMS operation, and KHM performed theoretical calculations. All authors commented on the manuscript.

Competing interests. The authors declare that they have no competing interests.

Acknowledgements. We thank the Caltech Facilities for their support in RECAP campaign. We thank Kristian H. Møller and Henrik G. Kjaergaard for calculation of dipole moments and polarizabilities. This work was supported by the NOAA Cooperative Agreement with CIRES, NA17OAR4320101. The NOAA Chemical Sciences Laboratory acknowledges support for this work from the California Air Resources Board under agreement number 20RD002.

References

Adams, N. G., Babcock, L. M., Mostefaoui, T. M., and Kerns, M. S.: Selected ion flow tube study of NH4+ association and of product switching reactions with a series of organic molecules, International Journal of Mass Spectrometry, 223-224, 459–471, https://doi.org/https://doi.org/10.1016/S1387-3806(02)00932-6, 2003.

Allen, H. M., Crounse, J. D., Kim, M. J., Teng, A. P., Ray, E. A., McKain, K., Sweeney, C., and Wennberg, P. O.: H2O2 and CH3OOH (MHP) in the Remote Atmosphere: 1. Global Distribution and Regional Influences, 127, e2021JD035 701, https://doi.org/https://doi.org/10.1029/2021JD035701, 2022.

Berndt, T., Scholz, W., Mentler, B., Fischer, L., Herrmann, H., Kulmala, M., and Hansel, A.: Accretion Product Formation from Self- and Cross-Reactions of RO2 Radicals in the Atmosphere, Angewandte Chemie International Edition, 57, 3820–3824, https://doi.org/doi:10.1002/anie.201710989, 2018.

Blake, R. S., Wyche, K. P., Ellis, A. M., and Monks, P. S.: Chemical ionization reaction time-of-flight mass spectrometry: Multi-reagent analysis for determination of trace gas composition, International Journal of Mass Spectrometry, 254, 85–93, https://doi.org/https://doi.org/10.1016/j.ijms.2006.05.021, 2006.

Breitenlechner, M., Fischer, L., Hainer, M., Heinritzi, M., Curtius, J., and Hansel, A.: PTR3: An Instrument for Studying the Lifecycle of Reactive Organic Carbon in the Atmosphere, Analytical Chemistry, 89, 5824–5831, https://doi.org/10.1021/acs.analchem.6b05110, 2017.

Breitenlechner, M., Novak, G. A., Neuman, J. A., Rollins, A. W., and Veres, P. R.: A versatile vacuum ultraviolet ion source for reduced pressure bipolar chemical ionization mass spectrometry, Atmos. Meas. Tech., 15, 1159–1169, https://doi.org/10.5194/amt-15-1159-2022, 2022.

Canaval, E., Hyttinen, N., Schmidbauer, B., Fischer, L., and Hansel, A.: NH4+ Association and Proton Transfer Reactions With a Series of Organic Molecules, 7, https://doi.org/10.3389/fchem.2019.00191, 2019.

Crounse, J. D., McKinney, K. A., Kwan, A. J., and Wennberg, P. O.: Measurement of Gas-Phase Hydroperoxides by Chemical Ionization Mass Spectrometry, Analytical Chemistry, 78, 6726–6732, https://doi.org/10.1021/ac0604235, 2006.

de Gouw, J. and Warneke, C.: Measurements of volatile organic compounds in the earth's atmosphere using proton-transfer-reaction mass spectrometry, Mass Spectrometry Reviews, 26, 223–257, https://doi.org/https://doi.org/10.1002/mas.20119, 2007.

de Gouw, J., Warneke, C., Karl, T., Eerdekens, G., van der Veen, C., and Fall, R.: Sensitivity and specificity of atmospheric trace gas detection by proton-transfer-reaction mass spectrometry, International Journal of Mass Spectrometry, 223-224, 365–382, https://doi.org/https://doi.org/10.1016/S1387-3806(02)00926-0, 2003.

Ehn, M., Thornton, J. A., Kleist, E., Sipila, M., Junninen, H., Pullinen, I., Springer, M., Rubach, F., Tillmann, R., Lee, B., Lopez-Hilfiker, F., Andres, S., Acir, I.-H., Rissanen, M., Jokinen, T., Schobesberger, S., Kangasluoma, J., Kontkanen, J., Nieminen, T., Kurten, T., Nielsen, L. B., Jorgensen, S., Kjaergaard, H. G., Canagaratna, M., Maso, M. D., Berndt, T., Petaja, T., Wahner, A., Kerminen, V.-M., Kulmala, M., Worsnop, D. R., Wildt, J., and Mentel, T. F.: A large source of low-volatility secondary organic aerosol, Nature, 506, 476–479, https://doi.org/10.1038/nature13032, 2014.

Goldstein, A. H. and Galbally, I. E.: Known and unexplored organic constituents in the earth's atmosphere, Environmental Science & Technology, 41, 1514–1521, https://doi.org/Doi 10.1021/Es072476p, 2007.

Hansel, A., Scholz, W., Mentler, B., Fischer, L., and Berndt, T.: Detection of RO2 radicals and other products from cyclohexene ozonolysis with NH4+ and acetate chemical ionization mass spectrometry, Atmospheric Environment, 186, 248–255, https://doi.org/https://doi.org/10.1016/j.atmosenv.2018.04.023, 2018.

Heinritzi, M., Simon, M., Steiner, G., Wagner, A. C., Kürten, A., Hansel, A., and Curtius, J.: Characterization of the mass-dependent transmission efficiency of a CIMS, Atmos. Meas. Tech., 9, 1449–1460, https://doi.org/10.5194/amt-9-1449-2016, 2016.

Huey, L. G., Hanson, D. R., and Howard, C. J.: Reactions of SF6- and I- with Atmospheric Trace Gases, The Journal of Physical Chemistry, 99, 5001–5008, https://doi.org/10.1021/j100014a021, 1995.

Iyer, S., Lopez-Hilfiker, F., Lee, B. H., Thornton, J. A., and Kurtén, T.: Modeling the Detection of Organic and Inorganic Compounds Using Iodide-Based Chemical Ionization, The Journal of Physical Chemistry A, 120, 576–587, https://doi.org/10.1021/acs.jpca.5b09837, 2016.

Khare, P., Krechmer, J. E., Machesky, J. E., Hass-Mitchell, T., Cao, C., Wang, J., Majluf, F., Lopez-Hilfiker, F., Malek, S., Wang, W., Seltzer, K., Pye, H. O. T., Commane, R., McDonald, B. C., Toledo-Crow, R., Mak, J. E., and Gentner, D. R.: Ammonium-adduct chemical ionization to investigate anthropogenic oxygenated gas-phase organic compounds in urban air, Atmos. Chem. Phys. Discuss., 2022, 1–39, https://doi.org/10.5194/acp-2022-421, 2022.

Krechmer, J., Lopez-Hilfiker, F., Koss, A., Hutterli, M., Stoermer, C., Deming, B., Kimmel, J., Warneke, C., Holzinger, R., Jayne, J., Worsnop, D., Fuhrer, K., Gonin, M., and de Gouw, J.: Evaluation of a New Reagent-Ion Source and Focusing Ion–Molecule Reactor for Use in Proton-Transfer-Reaction Mass Spectrometry, Analytical Chemistry, 90, 12 011–12 018, https://doi.org/10.1021/acs.analchem.8b02641, 2018.

Lee, B. H., Lopez-Hilfiker, F. D., Mohr, C., Kurtén, T., Worsnop, D. R., and Thornton, J. A.: An Iodide-Adduct High-Resolution Time-of-Flight Chemical-Ionization Mass Spectrometer: Application to Atmospheric Inorganic and Organic Compounds, Environmental Science & Technology, 48, 6309–6317, https://doi.org/10.1021/es500362a, 2014a.

Lee, B. H., Mohr, C., Lopez-Hilfiker, F. D., Lutz, A., Hallquist, M., Lee, L., Romer, P., Cohen, R. C., Iyer, S., Kurtén, T., Hu, W., Day, D. A., Campuzano-Jost, P., Jimenez, J. L., Xu, L., Ng, N. L., Guo, H., Weber, R. J., Wild, R. J., Brown, S. S., Koss, A., de Gouw, J., Olson, K., Goldstein, A. H., Seco, R., Kim, S., McAvey, K., Shepson, P. B., Starn, T., Baumann, K., Edgerton, E. S., Liu, J., Shilling, J. E., Miller, D. O., Brune, W., Schobesberger, S., D'Ambro, E. L., and Thornton, J. A.: Highly functionalized organic nitrates in the southeast United States: Contribution to secondary organic aerosol and reactive nitrogen budgets, Proceedings of the National Academy of Sciences, 113, 1516–1521, https://doi.org/10.1073/pnas.1508108113, 2016.

Lee, L., Teng, A. P., Wennberg, P. O., Crounse, J. D., and Cohen, R. C.: On Rates and Mechanisms of OH and O3 Reactions with Isoprene-Derived Hydroxy Nitrates, The Journal of Physical Chemistry A, 118, 1622–1637, https://doi.org/10.1021/jp4107603, 2014b.

Lerner, B. M., Gilman, J. B., Aikin, K. C., Atlas, E. L., Goldan, P. D., Graus, M., Hendershot, R., Isaacman-VanWertz, G. A., Koss, A., Kuster, W. C., Lueb, R. A., McLaughlin, R. J., Peischl, J., Sueper, D., Ryerson, T. B., Tokarek, T. W., Warneke, C., Yuan, B., and de Gouw, J. A.: An improved, automated whole air sampler and gas chromatography mass spectrometry analysis system for volatile organic compounds in the atmosphere, Atmos. Meas. Tech., 10, 291–313, https://doi.org/10.5194/amt-10-291-2017, 2017.

Lindinger, W., Hansel, A., and Jordan, A.: On-line monitoring of volatile organic compounds at pptv levels by means of proton-transfer-reaction mass spectrometry (PTR-MS) medical applications, food control and environmental research, International Journal of Mass Spectrometry and Ion Processes, 173, 191–241, https://doi.org/https://doi.org/10.1016/S0168-1176(97)00281-4, 1998.

Lopez-Hilfiker, F. D., Iyer, S., Mohr, C., Lee, B. H., D'Ambro, E. L., Kurtén, T., and Thornton, J. A.: Constraining the sensitivity of iodide adduct chemical ionization mass spectrometry to multifunctional organic molecules using the collision limit and thermodynamic stability of iodide ion adducts, Atmos. Meas. Tech., 9, 1505–1512, https://doi.org/10.5194/amt-9-1505-2016, 2016.

Müller, M., Piel, F., Gutmann, R., Sulzer, P., Hartungen, E., and Wisthaler, A.: A novel method for producing NH4+ reagent ions in the hollow cathode glow discharge ion source of PTR-MS instruments, International Journal of Mass Spectrometry, 447, 116 254, https://doi.org/https://doi.org/10.1016/j.ijms.2019.116254, 2020.

Nah, T., Ji, Y., Tanner, D. J., Guo, H., Sullivan, A. P., Ng, N. L., Weber, R. J., and Huey, L. G.: Real-time measurements of gas-phase organic acids using SF6- chemical ionization mass spectrometry, Atmos. Meas. Tech., 11, 5087–5104, https://doi.org/10.5194/amt-11-5087-2018, 2018.

Nguyen, T. B., Crounse, J. D., Schwantes, R. H., Teng, A. P., Bates, K. H., Zhang, X., St. Clair, J. M., Brune, W. H., Tyndall, G. S., Keutsch, F. N., Seinfeld, J. H., and Wennberg, P. O.: Overview of the Focused Isoprene eXperiment at the California Institute of Technology (FIXCIT): mechanistic chamber studies on the oxidation of biogenic compounds, Atmos. Chem. Phys., 14, 13 531–13 549, https://doi.org/10.5194/acp-14-13531-2014, 2014.

Nguyen, T. B., Crounse, J. D., Teng, A. P., St. Clair, J. M., Paulot, F., Wolfe, G. M., and Wennberg, P. O.: Rapid deposition of oxidized biogenic compounds to a temperate forest, Proceedings of the National Academy of Sciences, https://doi.org/10.1073/pnas.1418702112, 2015.

Pagonis, D., Sekimoto, K., and de Gouw, J.: A Library of Proton-Transfer Reactions of H3O+ Ions Used for Trace Gas Detection, Journal of the American Society for Mass Spectrometry, 30, 1330–1335, https://doi.org/10.1007/s13361-019-02209-3, 2019.

Robinson, M. A., Neuman, J. A., Huey, L. G., Roberts, J. M., Brown, S. S., and Veres, P. R.: Temperature dependent sensitivity of iodide chemical ionization mass spectrometers, EGUsphere, 2022, 1–17, https://doi.org/10.5194/amt-2022-295, 2022.

Ryerson, T. B., Andrews, A. E., Angevine, W. M., Bates, T. S., Brock, C. A., Cairns, B., Cohen, R. C., Cooper, O. R., de Gouw, J. A., Fehsenfeld, F. C., Ferrare, R. A., Fischer, M. L., Flagan, R. C., Goldstein, A. H., Hair, J. W., Hardesty, R. M., Hostetler, C. A., Jimenez, J. L., Langford, A. O., McCauley, E., McKeen, S. A., Molina, L. T., Nenes, A., Oltmans, S. J., Parrish, D. D., Pederson, J. R., Pierce, R. B., Prather, K., Quinn, P. K., Seinfeld, J. H., Senff, C. J., Sorooshian, A., Stutz, J., Surratt, J. D., Trainer, M., Volkamer, R., Williams, E. J., and Wofsy, S. C.: The 2010 California Research at the Nexus of Air Quality and Climate Change (CalNex) field study, 118, 5830–5866, https://doi.org/https://doi.org/10.1002/jgrd.50331, 2013.

Schwantes, R. H., Teng, A. P., Nguyen, T. B., Coggon, M. M., Crounse, J. D., St. Clair, J. M., Zhang, X., Schilling, K. A., Seinfeld, J. H., and Wennberg, P. O.: Isoprene NO3 Oxidation Products from the RO2 + HO2 Pathway, The Journal of Physical Chemistry A, https://doi.org/10.1021/acs.jpca.5b06355, 2015.

Sekimoto, K., Li, S.-M., Yuan, B., Koss, A., Coggon, M., Warneke, C., and de Gouw, J.: Calculation of the sensitivity of proton-transfer-reaction mass spectrometry (PTR-MS) for organic trace gases using molecular properties, International Journal of Mass Spectrometry, 421, 71–94, https://doi.org/https://doi.org/10.1016/j.ijms.2017.04.006, 2017.

Steiner, G., Jokinen, T., Junninen, H., Sipilä, M., Petäjä, T., Worsnop, D., Reischl, G. P., and Kulmala, M.: High-Resolution Mobility and Mass Spectrometry of Negative Ions Produced in a 241Am Aerosol Charger, Aerosol Science and Technology, 48, 261–270, https://doi.org/10.1080/02786826.2013.870327, 2014.

Su, T.: Parametrization of kinetic energy dependences of ion–polar molecule collision rate constants by trajectory calculations, 100, 4703–4703, https://doi.org/10.1063/1.466255, 1994.

Teng, A. P., Crounse, J. D., and Wennberg, P. O.: Isoprene Peroxy Radical Dynamics, J. Am. Chem. Soc., 139, 5367–5377, https://doi.org/10.1021/jacs.6b12838, 2017.

Vasquez, K. T., Crounse, J. D., Schulze, B. C., Bates, K. H., Teng, A. P., Xu, L., Allen, H. M., and Wennberg, P. O.: Rapid hydrolysis of tertiary isoprene nitrate efficiently removes NOx from the atmosphere, Proceedings of the National Academy of Sciences, 117, 33 011–33 016, https://doi.org/10.1073/pnas.2017442117, 2020.

Xiong, F., McAvey, K. M., Pratt, K. A., Groff, C. J., Hostetler, M. A., Lipton, M. A., Starn, T. K., Seeley, J. V., Bertman, S. B., Teng, A. P., Crounse, J. D., Nguyen, T. B., Wennberg, P. O., Misztal, P. K., Goldstein, A. H., Guenther, A. B., Koss, A. R., Olson, K. F.,

de Gouw, J. A., Baumann, K., Edgerton, E. S., Feiner, P. A., Zhang, L., Miller, D. O., Brune, W. H., and Shepson, P. B.: Observation of isoprene hydroxynitrates in the southeastern United States and implications for the fate of NOx, Atmos. Chem. Phys., 15, 11 257–11 272, https://doi.org/10.5194/acp-15-11257-2015, 2015.

Xu, L., Møller, K. H., Crounse, J. D., Kjaergaard, H. G., and Wennberg, P. O.: New Insights into the Radical Chemistry and Product Distribution in the OH-Initiated Oxidation of Benzene, Environmental Science & Technology, 54, 13 467–13 477, https://doi.org/10.1021/acs.est.0c04780, 2020.

Yuan, B., Koss, A., Warneke, C., Gilman, J. B., Lerner, B. M., Stark, H., and de Gouw, J. A.: A high-resolution time-of-flight chemical ionization mass spectrometer utilizing hydronium ions (H3O+ ToF-CIMS) for measurements of volatile organic compounds in the atmosphere, Atmos. Meas. Tech., 9, 2735–2752, https://doi.org/10.5194/amt-9-2735-2016, 2016.

Yuan, B., Koss, A. R., Warneke, C., Coggon, M., Sekimoto, K., and de Gouw, J. A.: Proton-Transfer-Reaction Mass Spectrometry: Applications in Atmospheric Sciences, Chemical Reviews, 117, 13 187–13 229, https://doi.org/10.1021/acs.chemrev.7b00325, 2017.

Zaytsev, A., Breitenlechner, M., Koss, A. R., Lim, C. Y., Rowe, J. C., Kroll, J. H., and Keutsch, F. N.: Using collision-induced dissociation to constrain sensitivity of ammonia chemical ionization mass spectrometry (NH4+ CIMS) to oxygenated volatile organic compounds, Atmos. Meas. Tech., 12, 1861–1870, https://doi.org/10.5194/amt-12-1861-2019, 2019.